The Discovery of Five Hot Jupiters by TESS

(article starts on next page)

The Astronomical Journal, 172:54 (23pp), 2026 July https://doi.org/10.3847/1538-3881/ae6449

The Discovery of Five Hot Jupiters by TESS*

Eike W. Guenther[1], William D. Cochran[2,3,4], Phillip J. MacQueen[2], Elisa Goffo[5], Hanna Kellermann[6], Benard Nsamba[7,8], Michael Endl[3], Daniel Sebastian[1,9], Davide Gandolfi[5], Cyrille Aumasson[10], Oscar Barragán[11], Slawomir Bednarz[12], Krzysztof Bernacki[12], Allyson Bieryla[13], Pau Bosch-Cabot[14], Ilaria Carleo[15,16], David R. Ciardi[17], Clark Catherine A. Clark[17], Szilard Csizmadia[18], Hans J. Deeg[19], Parker Duke[2], Gareb Enoc Fernández Rodríguez[19], Juliana Ehrhardt[6], Mark E. Everett[20], Malcolm Fridlund[21,22], Akihiko Fukui[19,23], Iskra Georgieva[24], Frank Grupp[6], Teruyuki Hirano[25,26,27], Petr Kabáth[28], Juma Kamulali[7,8,29], Yugo Kawai[30], John Kielkopf[31], Judith Korth[22,32], Lacedelli Gaia[19,33], Kristine W. F. Lam[34], David. W. Latham[13], John H. Livingston[35,36], Michael B. Lund[17], Priscilla Muheki[37], Felipe Murgas[19,33], Norio Narita[19,23,25,33], Greg Olmschenk[38], Enric Pallé[19], Carina M. Persson[39], Adam Popowicz[12], Teznie Pugh[2], Manfred Rätz[40], Seth Redfield[16], Arno Riffeser[6], Marek Skarka[28], Luisa Maria Serrano[5], Alexis M. S. Smith[18], Gregor Srdoc[41], Vincent Van Eylen[42], Julian Van Eyken[17], and Anäel Wünsche[10]

[1] Thüringer Landessternwarte Tautenburg, Sternwarte 5, 07778 Tautenburg, Germany
[2] McDonald Observatory, The University of Texas at Austin, Austin, TX 78712, USA
[3] Department of Astronomy, The University of Texas at Austin, Austin, TX 78712, USA
[4] Center for Planetary Systems Habitability, The University of Texas at Austin, Austin, TX 78712, USA
[5] Dipartimento di Fisica, Universita degli Studi di Torino, Via Pietro Giuria 1, I-10125, Torino, Italy
[6] Universitäts-Sternwarte München, Fakultät für Physik, Ludwig-Maximilians-Universität München, Scheinerstrasse 1, 81679, München, Germany
[7] Department of Physics, Faculty of Science, Kyambogo University, P.O. Box 1, Kyambogo, Kampala, Uganda
[8] Max-Planck-Institut für Astrophysik, Karl-Schwarzschild-Straße 1, D-85748 Garching, Germany
[9] School of Physics and Astronomy, University of Birmingham, Edgbaston, Birmingham B15 2TT, UK
[10] Observatoire des Baronnies Provençales, F-05150 Moydans, France
[11] Subdepartment of Astrophysics, Department of Physics, University of Oxford, Oxford OX1 3RH, UK
[12] Silesian University of Technology, Akademicka 16, Gliwice, Poland
[13] Center for Astrophysics, Harvard & Smithsonian, 60 Garden Street, Cambridge, MA 02138, USA
[14] Department of Physics and Astronomy, University of Lethbridge, Lethbridge, AB, T1K 3M4, Canada
[15] Instituto de Astrofísica de Canarias (IAC), E-38205 La Laguna, Tenerife, Spain
[16] Astronomy Department and Van Vleck Observatory, Wesleyan University, Middletown, CT 06459, USA
[17] California Institute of Technology, IPAC-NASA Exoplanet Science Institute, Pasadena, CA, USA
[18] Institute for Space Research, German Aerospace Center, 12489 Berlin, Germany
[19] Instituto de Astrofísica de Canarias, Via Lactea s/n, 38200, La Laguna, Tenerife, Spain
[20] NSF NOIRLab, 950 North Cherry Avenue, Tucson, AZ 85719, USA
[21] Leiden Observatory, University of Leiden, P.O. Box 9513, 2300 RA, Leiden, The Netherlands
[22] Department of Space, Earth and Environment, Astronomy and Plasma Physics, Chalmers University of Technology, 412 96 Gothenburg, Sweden
[23] Komaba Institute for Science, The University of Tokyo, 3-8-1 Komaba, Meguro, Tokyo 153-8902, Japan
[24] Department of Space, Earth and Environment, Chalmers University of Technology, Onsala Space Observatory, 439 92 Onsala, Sweden
[25] Astrobiology Center, 2-21-1 Osawa, Mitaka, Tokyo 181-8588, Japan
[26] National Astronomical Observatory of Japan, 2-21-1 Osawa, Mitaka, Tokyo 181-8588, Japan
[27] Department of Astronomical Science, School of Physical Sciences, The Graduate University for Advanced Studies (SOKENDAI), 2-21-1 Osawa, Mitaka, Tokyo 181-8588, Japan
[28] Astronomical Institute, Czech Academy of Sciences, Fričova 298, 25165 Ondřejov, Czechia
[29] 3Instituto de Astrofísica e Ciências do Espaço, Universidade do Porto, Rua das Estrelas, 4150-762 Porto, Portugal
[30] Department of Multi-Disciplinary Sciences, Graduate School of Arts andSciences, The University of Tokyo, 3-8-1 Komaba, Meguro, Tokyo153-8902, Japan
[31] Department of Physics and Astronomy, University of Louisville, Louisville, KY 40292, USA
[32] Division of Astrophysics, Department of Physics, Lund University, Box 43, 22100 Lund, Sweden
[33] Departamento de Astrof'ısica, Universidad de La Laguna (ULL), 38206 La Laguna, Tenerife, Spain
[34] Center for Astronomy and Astrophysics, TU Berlin, Hardenbergstraße 36, D-10623 Berlin, Germany
[35] Astrobiology Center, Japan National Astronomical Observatory of Japan, 2-21-1 Osawa, Mitaka, Tokyo 181-8588, Japan
[36] Astronomical Science Program, Graduate University for Advanced Studies, SOKENDAI, 2-21-1, Osawa, Mitaka, Tokyo, 181-8588, Japan
[37] Mbarara University of Science and Technology, P.O Box 1410, Mbarara, Uganda
[38] NASA Goddard Space Flight Center, USA
[39] Chalmers University of Technology, Department of Space, Earth and Environment, Onsala Space Observatory, 439 92 Onsala, Sweden
[40] Bundesdeutsche Arbeitsgemeinschaft für Veränderliche Sterne e.V., Germany Volkssternwarte Kirchheim e.V., Zur Sternwarte 1, D-99334 Amt Wachsenburg OT Kirchheim, Germany Privat Observatory Herges-Hallenberg, Germany
[41] Kotizarovci Observatory, Sarsoni 90, 51216, Viškovo, Croatia
[42] Mullard Space Science Laboratory, University College London, Holmbury St Mary, Dorking, Surrey RH5 6NT, UK
Received 2025 August 11; revised 2026 April 14; accepted 2026 April 15; published 2026 June 25

* Based on observations obtained with TESS.

Abstract

Despite decades of research on hot Jupiters, there are still several theories for their formation. Perhaps hot Jupiters form in several ways. Atmospheric and dynamical studies have the capability to constrain the formation scenarios. However, potential targets have to be well characterized before these observations can further constrain the theories. We present the confirmation and characterization of five hot and warm Jupiters discovered by the TESS space mission. Using TESS data combined with ground-based observations, we determine the masses, radii, and other parameters of TOI-2040 b, TOI-2049 b, TOI-2578 b, TOI-4427 b, and TOI-4458 b. Three of the planets have equilibrium temperatures of about 1800 K while two have temperatures of about 1000 K. Particularly interesting for future atmospheric characterizations are TOI-2578 b and TOI-4427 b, because of their low density and large transmission spectroscopy metric. TOI-4458 b is of special interest because it is in the northern PLATO field. It appears that TOI-2040 b has a small, but measurable eccentricity.

Unified Astronomy Thesaurus concepts: Exoplanet atmospheres (487)

1. Introduction

Prior to the discovery of 51 Peg b (M. Mayor & D. Queloz 1995) it was thought that gas-giant planets exist only at a large distance from the host star, beyond the so called "ice line," where volatile elements (e.g., H_2O, CH_4, and NH_3) can condense. The discovery that Jovian planets with orbital periods of less than 10 days exist was thus very surprising. Hot Jupiters (HJs) are gas-giant planets in the mass range between $\sim$0.1 and 13 $M_{\rm Jup}$ with orbital periods shorter than 10 days. While HJs are usually defined on the basis of their orbital periods, it has been suggested to define them on the basis of temperature. Warm Jupiters are referred to as giant planets with equilibrium temperatures below 1000 K; HJs are hotter (S. Müller & R. Helled 2023). For a solar-like stars, an equivalent temperature of 1000 K would correspond to an orbital period of about 3.2 days. Jovian planets with periods between 5 and 10 days have also been called "tropical" Jupiters (L. Yu et al. 2018).

Even after decades of research and the discovery of 1221 HJs,[43] several formation scenarios are still being discussed (R. I. Dawson & J. A. Johnson 2018). In the migration scenario, gas-giant planets form beyond the ice line (S. E. Dodson-Robinson et al. 2009) and then migrate inward. One possibility is that the migration occurs due to the tidal interaction of the planet with the protoplanetary disk during the formation period (D. N. C. Lin et al. 1996; W. R. Ward 1997; H. Tanaka et al. 2002; R. P. Nelson & J. C. B. Papaloizou 2004). The detection of gaps in protoplanetary disks is direct observational evidence that planets interact with the disk during the formation period (R. Dong et al. 2015). Disk-driven migration not only explains the formation of HJs but also the existence of resonant chains of planets (C. Charalambous et al. 2022). A particularly interesting case for a resonant chain is the TOI-216 system, which contains a Neptune-sized planet and a gas giant in a 2:1 mean motion resonance (R. I. Dawson et al. 2019; D. Nesvorný et al. 2022). Resonances and gaps in disks hence support the disk-migration scenario.

Another scenario is planet–planet interaction. Gravitational interactions in multiplanet systems can scatter planets into highly eccentric orbits which, if the periastron is sufficiently close to the host star, can be circularized by tidal interactions between the host star and the planet (F. A. Rasio & E. B. Ford 1996; S. Chatterjee et al. 2008; S. Naoz et al. 2011; Y. Wu & Y. Lithwick 2011; C. Beaugé & D. Nesvorný 2012; C. Petrovich 2015a). The multiplanet scattering scenario also explains the distribution of observed eccentricities (A. S. Libert & K. Tsiganis 2009). Eccentric orbits can also be the outcome of planet–disk interactions (P. Goldreich & R. Sari 2003). Other possibilities for high-eccentricity migration include Kozai–Lidov cycles (Y. Kozai 1962; M. L. Lidov 1962; Y. Wu & N. Murray 2003; C. Petrovich 2015b) or flyby encounters between two planetary systems in a cluster (D. Li et al. 2019a, 2020).

A prediction of the high-eccentricity migration scenario is that close-in planets should initially have eccentric orbits. But the orbits can be circularized by tidal interactions between the host star and the planet over time. Nevertheless, HJs with highly eccentric orbits have been found. For example, CoRoT-20 b has an eccentricity of $e = 0.59 \pm 0.02$. According to J. Rey et al. (2018) the currently high eccentricity of CoRoT-20 b is expected to be due to the presence of an outer brown dwarf companion with a mass of 17 $M_{\rm Jup}$, an orbital period of 1675^{+19}_{-17} days, and an eccentricity of $e = 0.60 \pm 0.03$. Another interesting system is WASP-107. The inner planet has an orbital period of 5.7 days, a Jupiter-like radius, and an exceptionally low density. The outer planet has an eccentric orbit, an orbital period of 1100 days, and at least the mass of Saturn. According to H. Yu & F. Dai (2024), high-eccentricity migration scenario can explain nearly all of these properties and they suggest that similar systems may also be the product of high-eccentricity migration.

Since in both migration scenarios HJs tend to clear out other planets from their orbital regions, they are generally predicted to be isolated (A. J. Mustill et al. 2015). However, isolated does not mean that there are no other planets in the system. Observations by H. A. Knutson et al. (2014) show that 51% $\pm$ 10% of HJs have companions with masses between 1 and 13 $M_{\rm Jup}$ and orbital semimajor axes between 1 and 20 au. The migration scenarios predict that the region through which the HJ has migrated should be cleared from planets. There is observational evidence that this is the case. For example, from the analysis of transit timing variations of 39 HJs observed by TESS, X.-Y. Wang et al. (2021) rule out companion planets with masses greater than 0.39–5.0 $M_\oplus$, 1.23–14.36 $M_\oplus$, 1.65–21.18 $M_\oplus$ and 0.69–6.75 $M_\oplus$ near the 1:2, 2:3, 3:2, and 2:1 resonances, respectively, with the HJ.

However, there are exceptions, such as WASP-47, a system that harbors an HJ sandwiched between an inner and an outer low-mass planet (J. C. Becker et al. 2015). Because of this special architecture, K. Batygin et al. (2016) have argued that this system could only have formed in situ.

[43] https://exoplanet.eu. Accessed 2026 March 8.

While there is observational evidence for all three migration scenarios, formation theories of HJs should not only explain the existence of short-period gas-giant planets, but also should reproduce their observed occurrence rates (J. N. Winn & D. C. Fabrycky 2015). Up to about a decade ago not even the occurrence rate of HJs around G stars was known. While this rate is now reasonably well established, details like the joint dependence on period, planet mass, and stellar mass remain not well determined.

Using data from the Kepler Space Telescope (Kepler), A. W. Howard et al. (2012) originally obtained an occurrence rate of 0. 4 ± 0.1% (for $8.0\,R_\oplus \leqslant R_\mathrm{p} \leqslant 22\,R_\oplus$ and $P < 10$ days) and F. Fressin et al. (2013) found 0.43% ± 0.05% (for $6.0\,R_\oplus \leqslant R_\mathrm{p} \leqslant 32\,R_\oplus$ and $0.8\,\mathrm{days} \leqslant P \leqslant 10$ days). These results were initially surprising, because the CoRoT space mission obtained a higher occurrence rate of 0.98% ± 0.26%. Furthermore, radial-velocity (RV) surveys also provided a higher occurrence rates: 1.2% ± 0.1% (G. Marcy et al. 2005), 1.5% ± 0.6% (A. Cumming et al. 2008), 0.89% ± 0.36% (M. Mayor et al. 2011), and 1.2% ± 0.38% (J. T. Wright et al. 2011). J. Wang et al. (2015) point out that the Kepler results were initially affected by photometric dilution and subgiant contamination making it difficult to draw firm conclusions. After reevaluating the Kepler result M. Beleznay & M. Kunimoto (2022) recently determined an occurrence rate of 0.98% ± 0.36% for HJs orbiting G-type stars. This is consistent with CoRoT and the RV surveys. T. Gan et al. (2024) find an occurrence rates of 0.55% ± 0.14% for HJs and $16.04\%^{+3.69\%}_{-2.34\%}$ for cold Jupiters at distances of 1–5 au for solar-like stars. Q. H. Tran et al. (2025) found a giant planet occurrence rate of $1.9\%^{+2.6\%}_{-1.4\%}$ within 2.5 au in a sample of 20–200 Myr old stars.

We can thus conclude that about 1% of solar-like stars host an HJ and that there are at least 10 times as many cold Jupiters with orbital periods of $P \gtrsim 1$ yr than HJs (E. A. Petigura et al. 2018). HJs are thus rare compared to cold Jupiters, and represent an extreme outcome of planet formation rather than the typical case.

A theoretical study by T. Hallatt & E. J. Lee (2020) shows that high-eccentricity migration alone is not sufficient to explain the occurrence rate and the eccentricity distribution of warm Jupiters. Apart from high-eccentricity migration, there has to be another channel how warm Jupiters form. Possibly, the same is also true for HJs, and there is more than one way for warm Jupiter formation.

A complete theory of planet formation not only has to explain the occurrence rate of HJs, but also its dependence on stellar mass. HJs orbiting M stars are rare (J. Kepler 1609; M. Endl et al. 2006; S. Sabotta et al. 2021; T. Gan et al. 2023; M. Pinamonti et al. 2022; R. I. Glusman et al. 2026) but gas giants orbiting around M stars with long orbital periods are not that rare (M. Endl et al. 2022). T. Gan et al. (2024) showed the occurrence rate between hot and cold Jupiters drops when the stellar mass rises from 0.8 to 1.4 $M_\odot$

The analysis of CoRoT, Kepler, and TESS data shows that the occurrence rate of HJs for early-type stars is lower than for solar-like stars (S. Sabotta et al. 2019; M. Beleznay & M. Kunimoto 2022; D. Sebastian et al. 2022). This result is surprising, because theories predict that HJs should be more common around early-type stars (C. Mordasini et al. 2012; Y. Hasegawa & R. E. Pudritz 2013).

Even after decades of research it is not clear how HJs form. It is most likely that one scenario alone is not sufficient to explain the diversity of HJs. The most favored model is a combination of disk migration, which initially often leads to resonant chains, with subsequent planet–planet interaction (R. Luque et al. 2023).

Hopes to clarify the situation now lie in abundance studies of exoplanets and their host stars. It was originally thought that the C/O ratio of exoplanets alone would tell us where and how HJs formed (K. I. Öberg et al. 2011). Gas giants that sweep up most of their atmospheres from disk gas outside of the water snow line were expected to have a C/O ratio of ∼1. Much smaller C/O ratios would be an indication of significant planetesimal enrichment interior to the CO snow line. The discovery that the inflated Saturn-mass planet HAT-P-18 b has C/O ratio of ∼0.3 is thus very interesting (G. Fu et al. 2022). However, the inversion from atmospheric abundances to planet formation now seems to be more complicated than originally thought (P. Mollière et al. 2022). Understanding the effects of different formation models is possible, provided that quantitative abundance measurements of different species of a sample of planets are available. Transit and eclipse observations already led to the detection of many different species in HJ atmospheres, but quantitative measurement of the abundances are still in their infancy (D. Shulyak et al. 2019).

This situation has changed dramatically as a result of the availability of high-resolution infrared spectrographs (J. L. Birkby et al. 2017), such as the James Webb Space Telescope (JWST; L. Alderson et al. 2023; Z. Rustamkulov et al. 2023). The Atmospheric Remote-sensing Infrared Exoplanet Large-survey (ARIEL) spacecraft mission, which is due to launch in 2029, will provide spectra of about 1000 planets, and many of them will be gas giants (G. Tinetti et al. 2016; L. Puig et al. 2018).

In order to make the best use of these new facilities, observers need to provide the community with a well-characterized sample of HJs. Since the variation of the transit depth is proportional to the scale height of the atmosphere, and the scale height is a function of the temperature, the mean molecular weight of the atmosphere and the surface gravity of the planet (C. A. Griffith 2014; D. Deming et al. 2019), we must determine these parameters prior to transmission spectroscopy observations. We also need to know whether the system just contains one HJ, or if it is a system containing additional planets. RV follow-up observations of transiting HJs are often stopped when the masses of the planets are determined. The number of RV measurements is often not sufficient to assess if the orbits of HJs are eccentric or not. For many systems with close-in giant planets we do not know whether they host outer planetary or stellar companions. What is needed is a well-characterized sample of HJs orbiting relatively bright stars that can then be observed with high-resolution infrared spectrographs like those on the JWST and ARIEL.

Here, we present this necessary complete characterization of five HJs and warm Jupiters and their host stars identified by the TESS space mission. The selection criteria for these objects were that host stars are relatively bright, and can well be observed from northern latitudes. In our analysis we let kept the eccentricities as a free parameter to be able to constrain it.

We combine the space-based transit photometry with ground-based follow-up observations—including high-resolution imaging, high-precision RV measurements, and ground-based transit photometry—to confirm the planetary nature of the transit signals, derive the fundamental parameters of the host stars, and determine the mass, radius, and the orbital parameters of the transiting HJs. The purpose is to increase the sample of well characterize hot gas-giant planets for future atmospheric studies. The planets are TOI-2040 b, TOI-2049 b, TOI-2578 b, TOI-4427 b, and TOI-4458 b.

2. Observing Facilities Used

2.1. Photometric Observations Obtained by TESS

TESS is a mission designed to detect exoplanets from space using the transit method (G. R. Ricker et al. 2014). The ExoFOP database (R. Akeson & J. Christiansen 2019) was used to select the targets. The data processing by the TESS Science Processing Operations Center (SPOC; J. M. Jenkins et al. 2016) included aperture photometry, flagging of low-quality data, removal of trends related to systematic sources (presearch data conditioning), and finally a search for transiting planets (J. M. Jenkins 2002, 2020; J. D. Twicken et al. 2018; J. Li et al. 2019b). The sectors analyzed are given in the section for each target. The cadence of the observations was two minutes. However, there is one exception. For TOI-2040, we also used the full-frame images (FFIs), which have a time sampling of 30 minutes. The data are available in the SPOC archive (D. A. Caldwell et al. 2020), which also provides the information how to cut out data around an object of interest in an FFI, access the metadata, and understand the file properties and units. We analyzed the FFIs for TOI-2040 using the same methods as described in L. Thomas et al. (2025).

Given the relatively large angular size of the TESS point-spread function (PSF), there are usually several faint stars within the PSF of TESS apart from the primary star. Thus it is necessary to observe the transits with ground-based telescopes to determine which star actually hosts the transit event. We used a number of different instruments for these transit verification observations, which are listed in the Appendix.

2.2. Seeing-limited Photometric Observations

Seeing-limited imaging was used to confirm that the transits is on the stars observed spectroscopically.

2.2.1. Telescopio Carlos Sánchez with MuSCAT2

The transit of TOI-2578 was observed on 2021 November 19 with the Telescopio Carlos Sánchez, which has an aperture of 1.52 m and is located in the Instituto de Astrofísica de Canarias' Teide Observatory, at the island of Tenerife, Spain. The telescope is equipped with MuSCAT2. MuSCAT2, has the capability of four-color simultaneous imaging in the g (400–550 nm), r (550–700 nm), i (700–820 nm), and zs (820–920 nm) bands. It has four 1024×1024 pixel CCDs, and a field of view of 7.4×7.4 arcmin^2 with a pixel scale of $0\farcs44$ pixel^{-1}. It has demonstrated photometric precisions of 0.057%, 0.050%, 0.060%, and 0.076% as rms residuals of 60 s binning in the g, r, i and zs bands, respectively, for the G0 V star WASP-12 ($V = 11.57 \pm 0.16$). The exposure times were 10, 15, 10 and 10 s for filters g, r, i, and z, respectively. The data were reduced with the pipeline described in H. Parviainen et al. (2020).

2.2.2. Keplercam

TOI-4458 was observed with Keplercam on the 1.2 m telescope at the Fred Lawrence Whipple Observatory (FLWO) at Mount Hopkins, Arizona. Keplercam is a 4096×4096 Fairchild CCD 486 detector, which has a field- of view of $23' \times 23'$ and an image scale of $0\farcs672$ pixel^{-1}. Light curves are obtained using an $I_{\rm p}$ filter. Data were reduced using standard IDL routines and aperture photometry was performed using AstroImage. Details of the data reduction are given in K. A. Collins et al. (2017).

2.2.3. 50 cm Moore CDK20N Telescope of the University of Louisville

The Moore CDK20N telescope has an aperture of 0.5 m. For the observations an STX 16803 camera one full transit an a rp-filter. The image scale of the camera is $0\farcs536$ pixel^{-1}.

2.2.4. 43 cm CDK17 Telescope of the Observatoire Des Baronnies Provençales

The CDK17 telescope of the Observatoire des Baronnies Provençales has an aperture of 43 cm. For the observations, the ZWO ASI6200 Pro Mono camera together with a clear or an R filter is used. The image scale of the camera is $0\farcs8316$ pixel^{-1}.

2.2.5. 40 cm Observatori Astronómic Albanya Telescope

The Observatori Astronómic Albanya telescope has an aperture of 40 cm. With the Moravian G4-9000 camera used, the image scale is $1\farcs44$ pixel^{-1}. For the observations an $I_{\rm c}$ filter was used.

2.2.6. 40 cm Telescope at the the Patashnick Voorheesville Observatory

The LCO-McD has an aperture of 40 cm. With the STX-6303 camera used, the image scale is $0\farcs57$ pixel^{-1}. For the observations an $I_{\rm p}$ filter was used.

2.2.7. 35.6 cm Celestron EdgeHD1400 of the Acton Sky Portal Observatory

The Celestron EdgeHD1400 telescope has an aperture 35.6 cm. Observation are taken with the $g_{\rm p}$ or $R_{\rm c}$ filter. The image scale is $0\farcs69$ pixel^{-1}.

2.3. High-resolution Imaging

High-resolution imaging is required in order to make sure that there are no other stars within the photometric aperture of the ground-based telescopes used for the transit observations. In the following, we describe the instrumentation that was used to observe the targets.

2.3.1. WIYN Telescope with NESSI

High-resolution speckle interferometry was obtained with the NESSI camera on the WIYN telescope at KPNO (S. B. Howell et al. 2021). A filter with a width of 40 nm centered at 832 nm was used for the observations. The scale is $0\farcs02$ pixel^{-1}.

2.3.2. Palomar–Hale Telescope with PALM-3000

The Hale telescope at Palomar Mountain is equipped PALM-3000, an adaptive optics (AO) system that has an infrared imager the can be used in the wavelength region from 1.6 to 2.2 μm (A. H. Bouchez et al. 2008). The scale of the images is 0.025 pixels arcsec^{-1}.

2.4. Spectroscopic Observations

Reconnaissance spectra, as well as RV measurements of the targets were obtained with the telescopes and spectrographs described in the following. The RV measurements are given in the Appendix: Table 5 for TOI-2040, Table 7 for TOI-2049, Table 6 for TOI-2578, Table 8 for TOI-4427, and Table 9 for TOI-4458.

2.4.1. Tillinghast Telescope with the TRES Spectrograph

The Tillinghast Reflector Echelle Spectrograph (TRES) is installed on the 1.5 m Tillinghast Telescope located at FLWO in southern Arizona, operated by the Center for Astrophysics, Harvard and Smithsonian. It achieves a resolving power of $R = 44{,}000$ over the wavelength range from 385.0 to 909.6 nm. The data pipeline for TRES is described in D. J. Mink (2011).

2.4.2. Alfred–Jensch Telescope with TCES Spectrometer

The Tautenburg Coudé Echelle Spectrograph (TCES) is installed on the 2 m Alfred–Jensch Telescope operated by Thüringer Landessternwarte Tautenburg. The instrument achieves a resolving power of $R = 67{,}000$ over the wavelength range from 460 to 730 nm. A temperature-stabilized I2 vapor absorption cell is placed in front of the slit, which provides a dense grid of absorption lines in the wavelength range 500–640 nm. Iodine lines are used to determine the instrumental shift during the observations. We used standard IRAF tools in order to reduce the spectra. The RV values were derived using the Velocity and Instrument Profile Estimator (M. Zechmeister et al. 2021; J. Köhler et al. 2025).

2.4.3. Fraunhofer Telescope with the FOCES Spectrograph

The Ludwigs–Maximilians–Universität München operates an observatory on the summit of Mount Wendelstein in the Bavarian Alps, which is equipped with a 210 cm Fraunhofer telescope. One of the instruments on that telescope is the Faser Optik Cassegrain Echelle Spektrograph (FOCES), known together with the laser frequency comb (LFC) as the Manfred Hirt Planet Spectrograph. In Table 9 we call this instrument FOCES. FOCES is a fiber-fed spectrograph that is placed in a temperature- and pressure-stabilized housing. The instrument achieves a resolving power of $R = 60{,}000$ and covers the wavelength range from 383 to 885 nm. Precise wavelength calibration is obtained with simultaneous reference using an LFC (L. Thomas et al. 2025). The FOCES spectra were reduced using the Munich Analyzer for RV Measurements with B-spline Optimized Templates (H. Kellermann et al. 2020).

2.4.4. Harlan J. Smith Telescope with the Robert G. Tull Spectrometer

The Robert G. Tull spectrograph is installed at the Coudé focus of the 2.72 m Harlan J. Smith telescope of McDonald Observatory operated by the University of Texas (R. G. Tull et al. 1995). The instrument is a cross-dispersed white pupil Echelle spectrograph. A 2048×2048 pixel CCD at the "F3" focal position, combined with a $1\farcs2$ wide entrance slit gives a resolving power of about 60,000 over the wavelength range of 375–1020 nm. A temperature-stabilized I2 vapor absorption cell placed in front of the slit provides the velocity metric. All data were reduced and extracted using an IRAF pipeline script. Precise RVs down to a few meters per second were computed using the Austral pipeline (M. Endl et al. 2000). We call this instrument McDonald in Tables 5, 6, 7, 8, 9.

2.4.5. WIYN Telescope with the NEID Spectrometer

Spectra from this instrument were used for determining the properties of the host stars TOI-2578 and TOI-4427. NN-explore Exoplanet Investigations with Doppler Spectroscopy (NEID) is an ultraprecise spectrometer which is fiber fed from the 3.5 m WIYN telescope located at KPNO (C. Schwab et al. 2016). NEID has a resolving power of $R = 110{,}000$ over the wavelength range from 380 to 930 nm. The instrument, the NEID Data Reduction Pipeline, and its performance have been described in S. Halverson et al. (2016) and A. F. Gupta et al. (2025).

2.4.6. Keck Telescope with the HIRES Spectrometer

Spectra from this instrument were used for determining the properties of TOI-20240. The HIRES spectrum was collected via the TESS–Keck Survey (A. Chontos et al. 2022). The Keck/HIRES spectrum was extracted and reduced with the standard MAKEE pipeline (T. Barlow 2024).

3. Analysis and Results

3.1. Deriving the Properties of the Host Stars and Their Planets

We determine the stellar parameters using four different methods so that we not only determine the statistical errors but also the systematic errors. The details of the methods used are described in Sections 3.1.1, 3.1.2, and 3.1.3. In Table 1, we list the parameters obtained, and we discuss the values obtained using the different methods in the sections about the individual objects. Within the errors, the radii, masses, and ages of the host stars derived by the different methods are the same. We thus averaged the values derived.

3.1.1. Stellar Parameters from ARIADNE and the Isochrones Code

The first method is the spectral energy distribution (SED) fitting algorithm ARIADNE developed by J. I. Vines & J. S. Jenkins (2022).[44] For this we used magnitudes from the literature which are given in Tables 2 and 3. ARIADNE limits the extinction (A_V) to the maximum line-of-sight value taken from the Galactic dust map of D. J. Schlegel et al. (1998), as recalibrated by E. F. Schlafly & D. P. Finkbeiner (2011).

The second method is the isochrones code (T. D. Morton 2015), which used Modules for Experiments in Stellar Astrophysics (MESA) isochrones (J. Choi et al. 2016; A. Dotter 2016).

This method utilities the multimodal nested sampler `multinest` (F. Feroz & M. P. Hobson 2008; F. Feroz et al. 2009, 2019) to sample 1000 live points with the following input: effective temperature, metallicity, and parallax, as well as stellar magnitudes in Tycho B, Tycho V,

[44] https://github.com/jvines/astroARIADNE

Table 1
Parameters of the Host Stars

Parameter	TOI-2040	TOI-2049	TOI-2578	TOI-4427	TOI-4458
Gaia DR3	2227309055469504640[a]	2009110972943346304[a]	271313363265864960[a]	1119137502311125248[a]	1654995798462043008[a]
TESS Input Catalog	427730490[a]	314835525[a]	104986789[a]	207339000[a]	229671380[a]
2MASS *J*	23290579+7130228[b]	23073832+5641402[b]	04321249+5215101[b]	09001170+7208524[b]	6483021+7445499[b]
Tycho Catalogue (TYC)	TYC 4486-00471-1[c]	4006-1797-1[c]	3354-237-1[c]	…	4426-400-1
R.A. (ICRS)[d]	23:29:05.9[c]	23:07:38.32[c]	04:32:12.50[c]	09:00:11.70[c]	16:48:30.24[c]
Decl. (ICRS)	+71:30:22.9[c]	+56:41:40.3[c]	+52:15:10.0[c]	+72:08:52.2[c]	+74:45:49.7[c]
pmRA (mas yr^{-1})	44.961 ± 0.016[a]	19.17 ± 0.012[a]	+4.334 ± 0.020[a]	37.396 ± 0.010[a]	−0.372 ± 0.015[a]
pmDecl (mas yr^{-1})	25.177 ± 0.015[a]	−0.548 ± 0.012[a]	−33.765 ± 0.015[a]	−19.870 ± 0.011[a]	−13.428 ± 0.013[a]
Parallax (mas)	6.9189 ± 0.0135[a]	1.754 ± 0.012[a]	3.561 ± 0.018[a]	4.957 ± 0.011[a]	1.938 ± 0.011[a]
Dist. (pc)	144.07[a]	$570.48^{+5.75}_{-3.94}$[a]	$279.80^{+2.31}_{-2.00}$[a]	$199.91^{+0.46}_{-0.40}$[a]	$504.39^{+2.13}_{-4.33}$[a]
Dist. (pc)	$146.3^{+1.8}_{-1.1}$[e]	595^{+34}_{-22}[e]	293^{+11}_{-8}[e]	$200.29^{+4.4}_{-1.8}$[e]	524^{+19}_{-18}[e]
Dist. (pc)	144.5 ± 1.1[f]	570.1 ± 3.8[f]	280.9 ± 1.3[f]	201.7	516.0[f]
Systemic RV (km s^{-1})	−20.30 ± 0.35[a]	−40.63 ± 0.40[a]	+59.05 ± 0.38[a]	−16.65 ± 46[a]	−53.84 ± 0.39[a]
Systemic RV (km s^{-1})	−19.93 ± 0.10[g, h]	−40.4[g, i]	+59.3[g, i]	−16.2[g]	−53.7[g,i]
T_{eff} (K)	5128 ± 100.0[g, h]	5750 ± 125[g, i]	6500 ± 125[g, i]	5500 ± 125[g,i]	5500 ± 125[g, i]
T_{eff} (K)	5486^{+231}_{-169}[e]	5700^{+224}_{-391}[e]	5811^{+200}_{-420}[e]	5759^{+99}_{-369}[e]	5952^{+77}_{-83}[e]
T_{eff} (K)	5132 ± 129[f]	6164 ± 202[f]	6333 ± 244[f]	5347 ± 135[f]	6151 ± 160[f]
log(*g*)	4.3 ± 0.1[g, h]	3.00 ± 0.25[g,i]	4.00 ± 0.25[g, i]	5.00 ± 0.25[g,i]	3.50 ± 0.25[g, i]
log(*g*)	$4.49^{+0.07}_{-0.09}$[e]	$3.52^{+0.46}_{-0.45}$[e]	$3.93^{+0.14}_{-0.16}$[e]	$4.45^{+0.15}_{-0.10}$[e]	$3.97^{+0.13}_{-0.17}$[e]
log(*g*)	4.515 ± 0.019[f]	3.669 ± 0.033[f]	4.473 ± 0.018[f]	[f]	3.96 ± 0.19[f]
[Fe/H]	+0.45 ± 0.06[g,h]	…	…	0.0 ± 0.25[g, i]	0.0 ± 0.25[g, i]
[Fe/H]	$-0.19^{+0.22}_{-0.23}$[e]	$-0.09^{+0.22}_{-0.25}$[e]	$-0.34^{+0.42}_{-0.28}$[e]	$-0.12^{+0.24}_{-0.34}$[e]	$+0.11^{+0.17}_{-0.14}$[e]
[Fe/H]	+0.300[f]	+0.311[f]	+0.01[f]	+0.002[f]	+0.170[f]
A_V	$0.45^{+0.16}_{-0.13}$[e]	$0.47^{+0.20}_{-0.21}$[e]	$0.48^{+0.16}_{-0.27}$[e]	$0.38^{+0.06}_{-0.03}$[e]	$0.04^{+0.06}_{-0.03}$[e]
A_V	0.042 ± 0.041	0.67 ± 0.11	0.70 ± 0.13	0.055 ± 0.042[f]	0.037 ± 0.036[f]
R_* ($R_\odot$)	0.87 ± 0.02	3.20 ± 0.01	1.64 ± 0.02	0.89 ± 0.03	1.96 ± 0.04
M_*($M_\odot$)	0.92 ± 0.03	1.57 ± 0.03	1.27 ± 0.09	0.90 ± 0.03	1.47 ± 0.04
Density (g cm^{-3})[j]	$1.90^{+0.14}_{-0.13}$	$0.0676^{+0.0014}_{-0.0014}$	$0.378^{+0.039}_{-0.035}$	$1.86^{+0.13}_{-0.15}$	$0.2^{+0.3}_{-0.2}$
Density (g cm^{-3})[k]	$1.96^{+0.13}_{-0.12}$	$0.0676^{+0.0014}_{-0.0014}$	$0.404^{+0.038}_{-0.037}$	$2.01^{+0.32}_{-0.64}$	$0.6^{+0.3}_{-0.3}$
L_* ($L_\odot$)	$0.60^{+0.12}_{-0.08}$	$12.7^{+2.8}_{-3.3}$	$3.30^{+0.69}_{-0.91}$	0.67 ± 0.04	$5.34^{+0.54}_{-0.50}$
Age (Gyr)	$8.7^{+2.8}_{-3.2}$	$2.2^{+0.4}_{-0.3}$	5.6 ± 1.6	7.9 ± 3.4	2.8 ± 0.3
v sin *i* (km s^{-1})	1.86 ± 1.0[g, h]	16.0 ± 2.0[g, i]	8.0 ± 2.0[g, i]	$0.0^{+2.0}_{-0.0}$	8.0 ± 2.0

Notes.
[a] SIMBAD.
[b] Two Micron All Sky Survey (2MASS).
[c] SIMBAD using Gaia data.
[d] International Celestial Reference System (ICRS).
[e] This work: ARIADNE.
[f] This work: isochrones code.
[g] ExoFOP.
[h] Keck/HIRES spectrum.
[i] TRES recon. spectrum.
[j] Computed using stellar models and machine learning.
[k] Obtained from transit light curve.
[l] Gaia Data Release 3 (DR3).

Sloan Digital Sky Survey (SDSS) *g*, SDSS *r*, SDSS *i*, *J*, *H*, *Ks*, W1, W2, W3, and *G*, if available for that star. The extinction is sampled uniformly as a free parameter.

As pointed out by J. Tayar et al. (2022) determinations of the stellar radius and mass have systematic uncertainty floor of 4.2% in radius, ∼5% in mass, 2.4% in temperature, ∼2.0% in luminosity, and ∼20% in age even for stars similar to the Sun, because of uncertainties in both the fundamental scale and our models of stellar evolution. We thus include the systematic errors together with the statistical ones in the error budget.

3.1.2. Stellar Parameters from ExoFOP

We also determined the stellar parameters from the echelle spectra using a spectroscopic fitting method that compares the observations to a large library of synthetic spectra (M. Endl & W. D. Cochran 2016) and the values derived from the reconnaissance spectroscopy by ExoFOP. The masses and radii of all host stars were already derived as part of the TESS follow-up campaign and are given in the ExoFOP database (R. Akeson & J. Christiansen 2019).

3.1.3. Stellar Parameters Using Computed Stellar Models and Machine Learning

We computed stellar models using the one-dimensional stellar evolution code MESA (B. Paxton et al. 2011, 2013, 2015, 2018, 2019) version r12778. The computed stellar model grid spans the parameter ranges of 0.6–1.8 $M_\odot$ in steps of 0.05 $M_\odot$; initial metallicity, [Fe/H], in the range between

Table 2
Magnitudes of the Host Stars TOI-2040, TOI-2049, and TOI-2578

Parameter	TOI-2040	TOI-2049	TOI-2578
TESS [mag]	11.067 ± 0.007[a]	10.66 ± 0.01[a]	10.586 ± 0.006[a]
B [mag]	12.2 ± 0.2[a]	12.1 ± 0.2[a]	11.9 ± 0.2[a]
V [mag]	11.17 ± 0.02[a]	11.41 ± 0.02[a]	11.35 ± 0.01[a]
Gaia [mag]	11.4796 ± 0.0003[b]	11.209 ± 0.02[b]	11.1208 ± 0.0007[b]
u [mag]	14.81 ± 0.008[a]	14.917 ± 0.007[a]	…
g [mag]	12.0573 ± 0.0007[a]	11.7604 ± 0.0007[a]	…
r [mag]	11.5192 ± 0.0007[a]	11.0887 ± 0.0007[a]	…
i [mag]	11.4059 ± 0.0008[a]	10.8536 ± 0.0006[a]	…
z [mag]	13.4267 ± 0.0145[a]	13.10 ± 0.01[a]	…
J [mag]	10.514 ± 0.018[c]	9.867 ± 0.02[c]	9.82 ± 0.02[c]
H [mag]	10.231 ± 0.015[c]	9.56 ± 0.02[c]	9.52 ± 0.02[c]
K [mag]	10.166 ± 0.022[c]	9.47 ± 0.02[c]	9.42 ± 0.02[c]
WISE[d] 3.4 μm [mag]	10.147 ± 0.023[a]	9.39 ± 0.02[a]	9.36 ± 0.02[a]
WISE 4.6 μm [mag]	10.189 ± 0.020[a]	9.43 ± 0.02[a]	9.38 ± 0.02[a]
WISE 12 μm [mag]	10.133 ± 0.044[a]	9.41 ± 0.04[a]	9.32 ± 0.4[a]
WISE 22 μm [mag]	9.0[a]	9.0 ± 0.4[a]	8.6 ± 0.4[a]

Notes.
[a] ExoFOP.
[b] Gaia DR3.
[c] 2MASS.
[d] Wide-field Infrared Survey Explorer (WISE).
[e] SIMBAD.
[f] This work: ARIADNE.
[g] This work: isochrones code.

Table 3
Magnitudes of the Host Stars TOI-4427 and TOI-4458

Parameter	TOI-4427	TOI-4458
TESS [mag]	11.343 ± 0.006[d]	11.67 ± 0.007[d]
B [mag]	12.80 ± 0.15[d]	12.2 ± 0.2[d]
V [mag]	11.98 ± 0.07[d]	11.2 ± 0.2[d]
Gaia [mag]	11.859 ± 0.0002[a]	11.4775 ± 0.0003[a]
u [mag]	…	14.8142 ± 0.0008
g [mag]	…	12.0573 ± 0.0009[d]
r [mag]	…	11.5192 ± 0.0. 0007[d]
i [mag]	…	11.4059 ± 0.0008[d]
z [mag]	…	13.427 ± 0.001[d]
J [mag]	10.624 ± 0.02[d]	10.51 ± 0.02[d]
H [mag]	10.237 ± 0.02[d]	10.23 ± 0.02[d]
K [mag]	10.163 ± 0.03[d]	10.17 ± 0.02[d]
WISE 3.4 μm [mag]	10.118 ± 0.02[d]	10.15 ± 0.02[d]
WISE 4.6 μm [mag]	10.183 ± 0.02[d]	10.19 ± 0.02[d]
WISE 12 μm [mag]	10.236 ± 0.2[d]	10.13 ± 0.04[d]
WISE 22 μm [mag]	8.617[d]	9.0[d]

Notes.
[a] Gaia DR3.
[b] SIMBAD.
[c] 2MASS.
[d] ExoFOP.

-0.50 and 0.50 dex in steps of 0.1 dex; and the helium enrichment ratio, $\Delta Y/\Delta Z$, from 0.4 to 2.8. The initial helium mass fraction, Y_i is determined following

$$Y_i = \frac{\Delta Y}{\Delta Z} Z_i + Y_0,$$

where Z_i is the initial metal mass fraction and Y_0 is the primordial Big Bang nucleosynthesis helium mass fraction value, taken as 0.2484 (R. H. Cyburt et al. 2003). The physics of the stellar model grid is described in B. Nsamba et al. (2025).

In order to infer the exoplanet host star properties (mass, radius, and age), we make use of the recently developed machine learning tool Machine Learning Algorithm for Inferring Stellar Parameters (J. Kamulali et al. 2025), which employs a stacked regressor (D. Wolpert 1992; L. Breiman 1996). The stacking regressor was shown to infer the most accurate model parameters during the intensive performance testing of various approaches highlighted in J. Kamulali et al. (2025). The predictions of exoplanet host star properties inferred using the stacking regressor were based on individual inferences made from the base regressors, i.e., extremely randomized trees regressor (L. Wehenkel et al. 2006), random forest regressor (L. Breiman 2001), extreme gradient boosting (J. H. Friedman 2001), and categorical boosting (L. Prokhorenkova et al. 2017).

The individual inferences were combined using a simple linear regression (meta learner) through weighting based on the least squares optimization method (C. L. Lawson & R. J. Hanson 1995) to yield the final predictions. The model training was based on atmospheric properties (mainly effective temperature, metallicity, and luminosity).

We propagated the errors to the fundamental properties of the planet's host stars by drawing 10,000 random samples within the measurement uncertainties on the effective temperature, metallicity, and luminosity. The distributions of the predictions were used to compute the median, 16th, and 84th percentiles, which together give the 68% confidence interval. The stellar parameters derived are given in Table 1.

3.1.4. Adopted Values for the Masses and Radii of the Host Stars

The errors of the stellar mass and radius errors directly propagate to the mass and radius determination of the planets.

Table 4
Parameters of the Planets

Parameter	TOI-2040 b	TOI-2049 b	TOI-2578 b	TOI-4427 b	TOI-4458 b
$T_0 - 2450000$	$9740.36547^{+0.00015}_{-0.00016}$	$8768.846^{+0.011}_{-0.012}$	$9911.48030^{+0.00064}_{-0.00062}$	$9598.7129540^{+0.00016}_{-0.00016}$	$9711.66523^{+0.00020}_{-0.00021}$
P [days]	$3.8608576^{+0.0000045}_{-0.0000044}$	$5.303468^{0.000050}_{-0.000048}$	$3.4579667^{+0.0000033}_{-0.0000033}$	$4.6182621^{+0.0000017}_{-0.0000017}$	$3.9393792^{+0.0000018}_{-0.0000018}$
Depth [ppm]	11569^{+215}_{-212}	2275^{+224}_{-202}	$11511.6467055^{+323}_{-300}$	$18614.3353254^{+236}_{-257}$	3368^{+21}_{-21}
T_{tot} [hr]	$2.657^{+0.016}_{-0.015}$	$4.915^{+0.20}_{-0.19}$	$2.623^{+0.026}_{-0.026}$	$2.655^{+0.014}_{-0.014}$	$5.753^{+0.013}_{-0.013}$
$u_{1,TESS}$	$0.474^{+0.133}_{-0.126}$	$0.42^{+0.37}_{-0.29}$	$0.37^{+0.12}_{-0.11}$	$0.45^{+0.13}_{-0.12}$	$0.348^{+0.042}_{-0.043}$
$u_{2,TESS}$	$0.14^{+0.12}_{-0.12}$	$0.14^{+0.37}_{-0.29}$	$0.120^{+0.11}_{-0.098}$	$0.12^{+0.12}_{-0.12}$	$0.159^{+0.077}_{-0.072}$
R_p/R_*	$0.10756^{+0.00100}_{-0.00099}$	$1.49^{+0.071}_{-0.067}$	$0.1073^{+0.0014}_{-0.0014}$	$0.1073^{+0.0015}_{-0.0014}$	$0.05804^{+0.00018}_{-0.00018}$
a [au]	$0.04730^{+0.0015}_{-0.0015}$	$0.06919^{+0.00052}_{-0.00052}$	$0.0495^{+0.0022}_{-0.0021}$	$0.05389^{+0.0052}_{-0.0035}$	$0.0522^{+0.0016}_{-0.0015}$
b [au]	$0.298^{+0.0.074}_{-0.108}$	$0.883^{+0.017}_{-0.024}$	$0.879^{+0.00856}_{-0.010}$	$0.61884^{+0.019}_{-0.021}$	$0.055^{+0.064}_{-0.039}$
i [deg]	$88.48^{+0.54}_{-0.36}$	$78.85^{+0.41}_{-0.70}$	$81.32^{+0.56}_{-0.65}$	$87.40^{+0.42}_{-0.35}$	$89.46^{+0.38}_{-0.61}$
e	$0.109^{+0.021}_{-0.020}$	$0.054^{+0.068}_{-0.038}$	$0.098^{+0.043}_{-0.042}$	$0.074^{+0.077}_{-0.052}$	$0.03^{+0.024}_{-0.020}$
ω	11^{+14}_{-15}	39^{+64}_{-126}	83^{+40}_{-37}	-75^{+167}_{-52}	-83^{+27}_{-31}
T_{eq} [K][a]	1070^{+29}_{-29}	1869^{+128}_{-128}	1778^{+75}_{-74}	1040^{+46}_{50}	1759^{+30}_{-31}
λ[b]	171^{10}_{-10}	119^{+18}_{-16}	$36.2^{+5.3}_{-5.0}$	$48.8^{+7.5}_{-7.6}$	192^{+12}_{-11}
Insolation [$F_\oplus$]	216^{+25}_{-23}	2032^{+619}_{-503}	1667^{+298}_{-259}	195^{+36}_{-35}	1595^{-111}_{+113}
TSM[c]	$26.2^{+1.8}_{-1.7}$	$7.4^{+1.6}_{-1.3}$	815^{+135}_{-109}	147^{+28}_{20}	$6.79^{+0.43}_{-0.39}$
R_p [R_{Jup}]	$0.921^{+0.023}_{-0.023}$	$1.485^{+0.071}_{-0.067}$	$1.754^{+0.058}_{-0.057}$	$1.168^{+0.028}_{-0.028}$	$1.107^{+0.023}_{-0.023}$
M_p [M_{Jup}]	$0.781^{+0.036}_{-0.036}$	$1.53^{+0.18}_{-0.18}$	$0.526^{+0.071}_{-0.068}$	$0.276^{+0.039}_{-0.041}$	$1.737^{+0.095}_{-0.095}$
ρ_p [g m^{-3}]	$1.24^{+0.11}_{-0.10}$	$0.578^{+0.114}_{-0.099}$	$0.121^{+0.021}_{-0.019}$	$0.214^{+0.036}_{-0.034}$	$1.59^{+0.14}_{-0.13}$
K [m s^{-1}]	$107.5^{+4.8}_{-4.7}$	130^{+15}_{-15}	$60.0^{+7.8}_{-7.6}$	$36.3^{+5.1}_{-5.4}$	$173.0^{+8.8}_{-9.0}$
offset$_{McDo}$ [m s^{-1}]	$15,813.5^{+3.4}_{-3.2}$	$-35,604^{+11}_{-11}$	$36,618.3^{+9.7}_{-9.8}$	$-48,573.2^{+4.5}_{-4.3}$	$5469.0^{+8.0}_{-6.5}$
offset$_{TRES}$ [m s^{-1}]	$-8.2^{+1.3}_{-1.3}$	…	$-94.9^{+7.8}_{-7.7}$	$-52.4^{+7.7}_{-8.1}$	…
offset$_{TCES}$ [m s^{-1}]	…	…	$339.4^{+36.9}_{-37.6}$	…	327^{+23}_{-24}
offset$_{FOCES}$ [m s^{-1}]	…	…	…	…	$-2.7^{+5.4}_{-5.4}$
jit$_{McDo}$ [m s^{-1}]	$9.0^{+6.0}_{-7.0}$	52^{+11}_{-11}	$39.6^{+9.1}_{7.2}$	$3.2^{+2.2}_{-3.3}$	28^{+11}_{-14}
jit$_{TRES}$ [m s^{-1}]	$4.0^{+12.0}_{-3.3}$	…	$9.8^{+15.1}_{-8.6}$	$4.5^{+11.7}_{-3.7}$	…
jit$_{TCES}$ [m s^{-1}]	…	…	$7.0^{+27}_{-6.0}$	…	33^{+58}_{-30}
jit$_{FOCES}$ [m s^{-1}]	…	…	…	…	$38.0^{+5.2}_{-4.4}$

Notes.
[a] Albedo = 0.
[b] λ: Jeans escape parameter (L. Fossati et al. 2017).
[c] Transmission spectroscopy metric (TSM; E. M. R. Kempton et al. 2018).

However, the errors given by the various algorithms are often only statistical errors but not systematic errors.

J. Tayar et al. (2022) show that the accuracies of stellar parameters are limited by uncertainties in both the fundamental scale and our models of stellar evolution, even for stars similar to the Sun. They find that the fundamental limit is about 4.2% in radius and about 5% in mass. These values were also used by V. M. Passegger et al. (2024). Recently, S. Morrell et al. (2026) showed that a model-independent accuracy of 2% in radius and 10% in mass can be achieved for exoplanet host stars using transit light curves, stellar SEDs, and archival photometry. An interesting aspect of this work is that the high accuracy of the radius determination is achieved using the distances obtained by Gaia and the SEDs. An important source of systematic errors is the methods used. We use several different methods to obtain the mass and radius of the star including two SED fitting methods. We find that the values obtained using the different methods agree very well. Within the errors, the masses and radii of the host stars are the same. The errors for evolved stars are larger than for main-sequence stars. We furthermore verify that the stellar parameters used are consistent with the Gaia distances. The adopted values given in Table 1 are the weighted averages that were obtained with the different methods. For completeness, we also list the nonweighted errors in the text. We use the values obtained by J. Tayar et al. (2022) as floors for the accuracy that can be achieved.

3.1.5. The Masses and Radii of the Planets

The masses and radii of all planets were derived by combining the masses and radii of the stars with all RV measurements obtained, and with the TESS light curves of the transit and the stellar parameters given in Table 1. The data (transit light curves from TESS, if available and RV measurements of various instruments) have been processed performing a joint maximum likelihood fit (Minuit; F. James & M. Roos 1975) with subsequent Markov Chain Monte Carlo (MCMC) sampling using `emcee` (D. Foreman-Mackey et al. 2013). For modeling both light curves and RVs, we used the Python package `starry` (R. Luger et al. 2019).

We use the following parameters for our model: time of transit T_0, orbital period P, planetary radius R_p, mass M_* and radius of the host star R_*, orbital inclination i, eccentricity e, longitude of periastron ω, and mass of the exoplanet M_p. Finally, we allow for an RV offset for each instrument and an overall linear trend of the RV. A prior for the limb-darkening parameterization (quadratic limb darkening) is obtained using `LDTk` (H. Parviainen & S. Aigrain 2015).

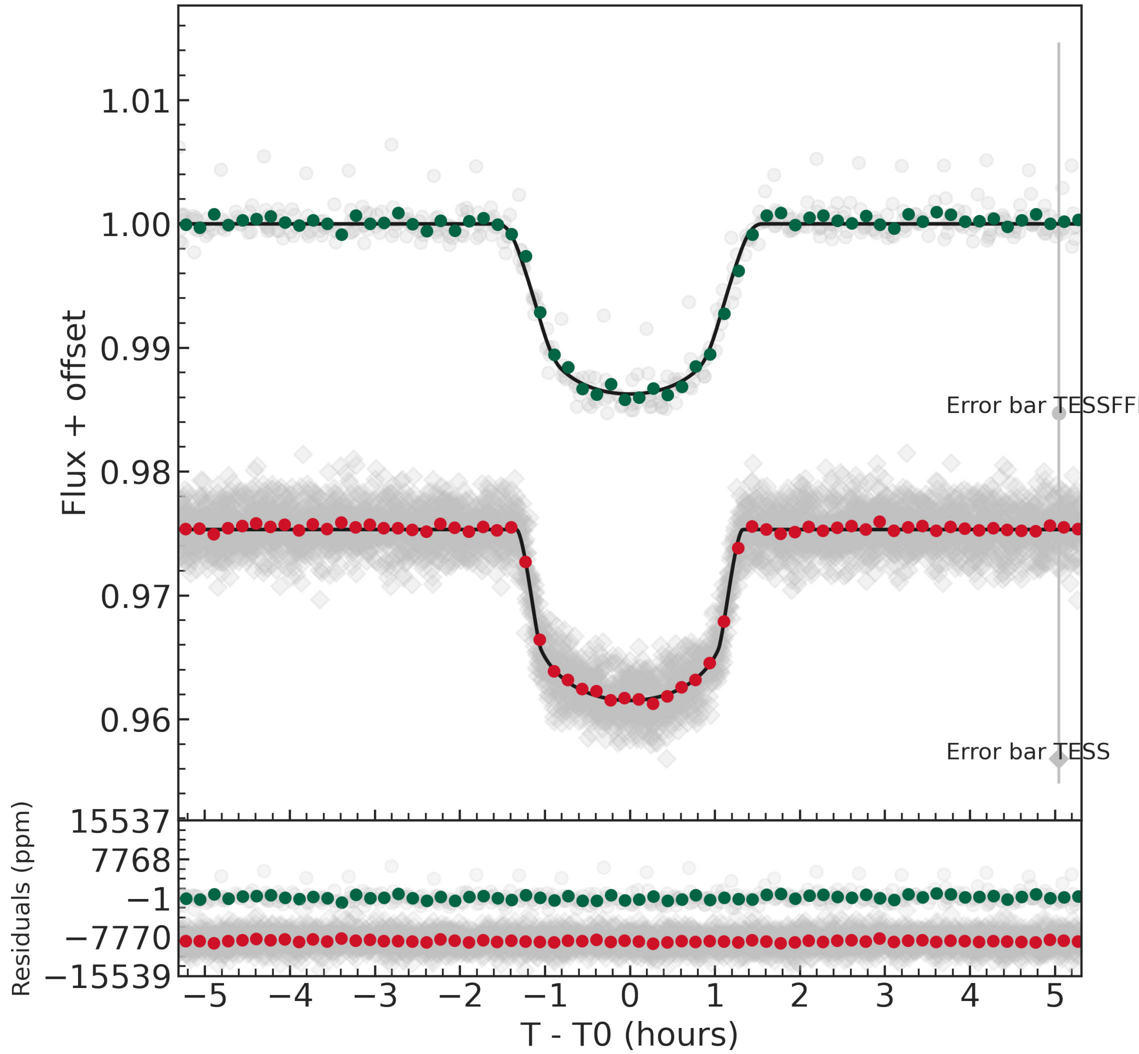

Figure 1. Phase-folded light curve obtained with TESS of TOI-2040 showing the phase-folded transit. The green line is the light curve obtained from the FFIs, and the red curve is from the extracted light curve. The residuals are shown in the bottom panel.

We also used the PYANETI code to determine the masses and radii of the planets (O. Barragán et al. 2019, 2022). The code uses a Bayesian approach combined with MCMC sampling to estimate the parameters of the planetary systems. By applying two different methods to the same data allows us to estimate the uncertainties of the algorithms. However, we find that both codes give almost the same results. The difference of the values derived using the two codes are smaller than the statistical errors. We therefore list in Table 4 only one set of results to ensure that all values are derived using the same algorithm. We decided for the values derived with PYANETI, because that code has been used for many other planets as well.

3.1.6. TOI-2040 b

TOI-2040 was observed by TESS in Sectors 17, 18, 24, 25, 52, and 58. The planet has an orbital period of about 3.86 days. Full transit observations were obtained with the 28 cm Celestron C11 at Volkssternwarte Kirchheim, the 30 cm telescope of the Silesian University of Technology, the 43 cm CDK17 telescope of the Observatoire des Baronnies Provençales, and the 50 cm Moore CDK20N telescope of the University of Louisville. These observations confirm that the transit is on target. The estimated PSF of the transit observations is between 4$''\!.$4 and 6$''$. The result of these observations was that the transit was detected and is on target. The stellar parameters are given in Table 1.

We derived the stellar parameters using the different methods described above. The masses, radii, and ages derived using the different methods are consistent. As part of the ExoFOP follow-up observations, a spectrum with the Keck telescope and the HIRES spectrograph was obtained on 2020 June 29, and five spectra were obtained with TRES on 2021 December 5 and 2021 December 7. The stellar radius given in ExoFOP (R. Akeson & J. Christiansen 2019) is $0.92 \pm 0.06\,R_\odot$. We find $0.87^{+0.02}_{-0.04}\,R_\odot$ using ARIADNE (J. I. Vines & J. S. Jenkins 2022), $0.87 \pm 0.04\,R_\odot$ using the isochrones code, and $0.915^{+0.041}_{-0.039}\,R_\odot$ using the computed stellar models and machine learning.

ExoFOP gives a mass of $0.93 \pm 0.03\,M_\odot$. We find $0.93^{+0.04}_{-0.05}$ $M_\odot$ (ARIADNE), $0.90 \pm 0.05\,M_\odot$ (isochrones code), and $0.915^{+0.041}_{-0.039}\,M_\odot$ using the computed stellar models and machine learning. The stellar parameters obtained with these methods are within the errors, i.e., the same.

We obtain $R_* = 0.87 \pm 0.02\,R_\odot$ and $M_* = 0.92 \pm 0.03\,M_\odot$ after averaging the individual values, except for the ExoFOP,

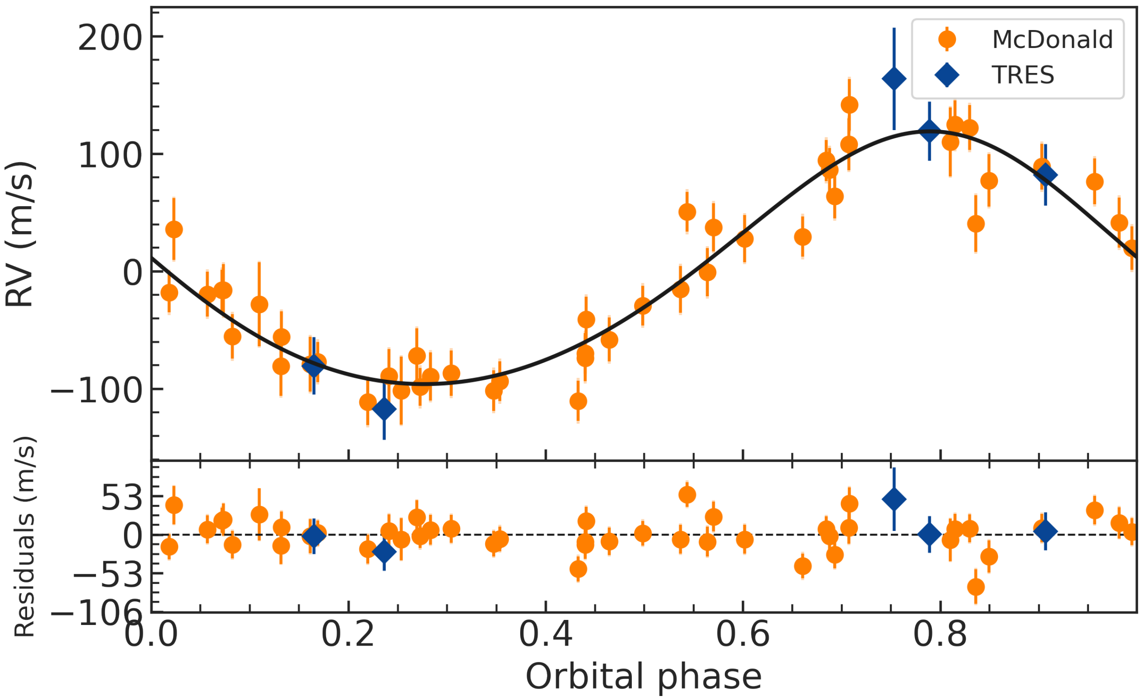

Figure 2. Phase-folded RV curve of TOI-2040 b with the orbital fit.

which we use only for comparison. The distances calculated using these stellar parameters are also consistent with the Gaia distance.

The phase-folded light curve obtained by TESS is shown in Figure 1. The green line is the light curve obtained from the FFIs, and the red curve is from the extracted light curve. The mass of TOI-2040 b was derived by combining the mass of the star with the RV measurements obtained with TRES spectrograph at the Tillinghast telescope and with the Robert G. Tull spectrometer at the Harlan J. Smith telescope at McDonald Observatory. We have found a significant eccentricity of $0.105^{+0.019}_{-0.019}$ with the MCMC algorithm, and $0.109^{+0.021}_{-0.020}$ with PYANETI. The orbit eccentricity is more than 5σ different from zero. The phase-folded RV curve is shown in Figure 2. The results obtained are given in Table 4.

3.1.7. TOI-2049 b

TOI-2049 b has an orbital period of 5.303 days. It was observed by TESS in Sectors 17, 18, 24, 25, and 52. The planet has an orbital period of 5.303 days. Reconnaissance spectra of TOI-2049 were obtained with TRES. We determine the stellar parameters of TOI-2049 using the same methods as described in Section 3.1. The stellar magnitudes are given in Table 2.

For the stellar radius measurements, we find $3.63^{+0.28}_{-0.18}\,R_\odot$ (ARIADNE), $3.3 \pm 0.1\,R_\odot$ (isochrones code), and $3.2^{+0.010}_{-0.011}\,M_\odot$ (computed stellar models and machine learning). The derived masses are $1.56^{+0.14}_{-0.11}\,M_\odot$ (ARIADNE), $1.85 \pm 0.14\,R_\odot$ (isochrones code), and $1.556^{+0.033}_{-0.040}\,M_\odot$ (computed stellar models and machine learning). The stellar parameters obtained photometrically and spectroscopically are the same, within the errors. Averaging the values, we obtain $R_* = 3.20 \pm 0.01\,R_\odot$ and $M_* = 1.57 \pm 0.03\,M_\odot$. The distance calculated using these stellar parameters is also consistent with the Gaia distance. The mass of the star obtained with the different methods agrees very well, but the errors are relatively large. This is because the star is evolved. The stellar parameters derived are given in Table 1.

The mass of the TOI-2049 b was derived by combining the mass of the star with the RV measurements obtained with the Robert G. Tull spectrometer at the Harlan J. Smith telescope at McDonald Observatory. The parameters derived for the planet are given in Table 4. The phase-folded light curve is shown in Figure 3 and the phase-folded RV curve in Figure 4.

3.1.8. TOI-2578 b

TOI-2578 b has an orbital period of 3.46 days. However, a stellar companion with a separation of $0\overset{''}{.}885 \pm 0\overset{''}{.}004$ that is 4.435 ± 0.049 mag fainter at 2166 nm (Brγ) was detected with the AO system of the 5 m Palomar–Hale telescope. Companions with a Δm smaller than 5.898 mag at separations larger than $0\overset{''}{.}5$ are excluded. Speckle observations at 562 nm and 832 nm with NESSI were obtained with the 3.5 m WIYN telescope. These images do not show a secondary source. These observations exclude companions with $\Delta m \geqslant 4.59$ mag and $\Delta m \geqslant 4.92$ mag with separations larger than $0\overset{''}{.}5$. Further AO observations were also obtained with the Shane near-IR AO system at the 3 m Shane telescope, with the same results.

Since the object was not detected in the optical observations, it is probably quite red, and thus does not affect the photometry and spectroscopy in the optical. Assuming the companion is bound to TOI-2578, it has to be an about $0.4\,M_\odot$ M dwarf, given the magnitude difference. While this star does not cause a problem for the optical observations it might be important for the dynamical history of HJ systems, as we will discuss below.

A full transit was observed with MuSCAT2 (N. Narita et al. 2019; Figure 5). Another full transit and the ingress was observed with the 35.6 cm Celestron of the Acton Sky Portal

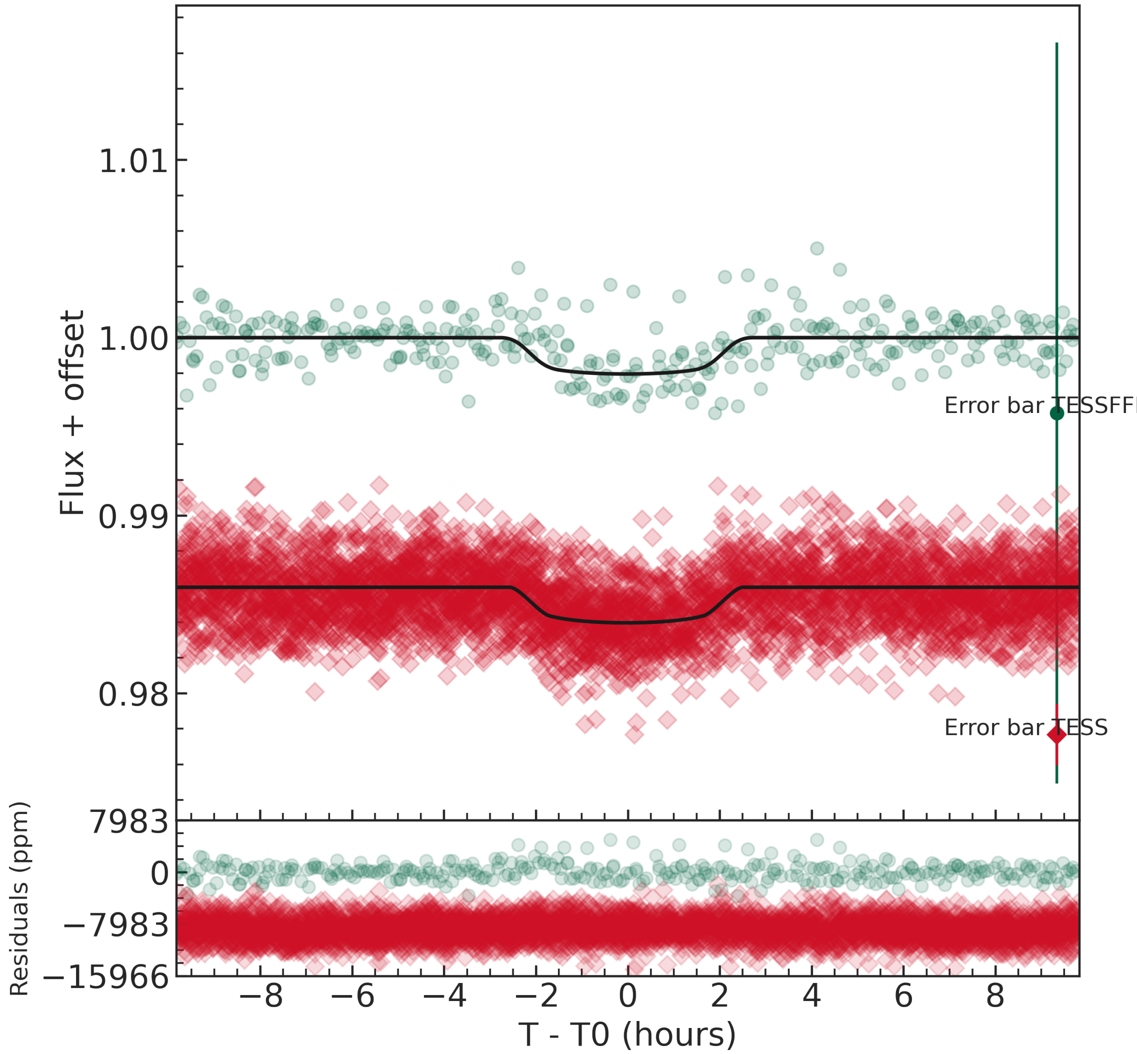

Figure 3. Phase-folded light curve of TOI-2049 b obtained by TESS with the best fit.

Observatory. Both observations confirm the transit to be on source.

The parameters derived for the host star are given in Table 1 and for the planet in Table 4. The stellar magnitudes are given in Table 2. As before we derived the stellar parameters using several methods. We find a stellar radius of $1.78^{+0.15}_{-0.06}\,R_\odot$ using ARIADNE, $1.64 \pm 0.07\,R_\odot$ using the isochrones code, and $1.634^{+0.0138}_{-0.0145}\,R_\odot$ using the computed stellar models and machine learning. For the stellar mass, we find $1.32^{+0.10}_{-0.08}\,M_\odot$ using ARIADNE, $1.30 \pm 0.09\,M_\odot$ using the isochrones code, and $1.172^{+0.114}_{-0.094}\,M_\odot$ from the computed stellar models and machine learning. The stellar parameters obtained photometrically and spectroscopically agree within the errors.

Averaging the values, we obtain $R_* = 1.64 \pm 0.02\,R_\odot$ and $M_* = 1.27 \pm 0.09\,M_\odot$.

We determined the mass of TOI-2578 b by combining the mass of the star with the RV measurements obtained with the Robert G. Tull spectrometer at the 2.7 m Harlan J. Smith telescope at McDonald Observatory, the TRES spectrograph at the Tillinghast telescope, and with TCES spectrometer at the Alfred–Jensch Telescope. We find that the eccentricity is $0.0939^{+0.028}_{-0.029}$ and thus significantly different from zero. The phase-folded light curve is shown in Figure 6, and the phase-folded RV curve in Figure 7.

3.1.9. TOI-4427 b

TOI-4427 was observed by TESS in Sectors 14, 20, 40, 47, 53, and 60. The orbital period of this planet, as derived from the TESS data, is 4.618 days. Speckle observations were obtained with NESSI on the 3.5 m WIYN telescope. These observations exclude companions with $\Delta m \geqslant 4$ mag with separations larger than $0\farcs3$ at 832 nm.

Transit observations were obtained with the Volkssternwarte Kirchheim with the Celestron C11, at the Silesian University of Technology with the 30 cm telescope, at the Observatoire des Baronnies Provençales with the 43 cm telescope, and at the Patashnick Voorheesville Observatory with the 40 cm telescope. The estimated PSF of the transit observations is between $2\farcs8$ and $3\farcs9$. These observations confirm that the transit is on source.

We determine the stellar parameters with the same methods as for the other stars. The parameters derived for the host star are given in Table 1. The brightness of the star is given in Table 3.

For the stellar radius measurements, we find $0.87 \pm 0.03\,R_\odot$ (ARIADNE), $0.87 \pm 0.05\,R_\odot$ (isochrones code), and $0.908^{+0.045}_{-0.042}\,R_\odot$ (computed stellar models and machine learning). The derived masses are $0.93 \pm 0.05\,M_\odot$ (ARIADNE),

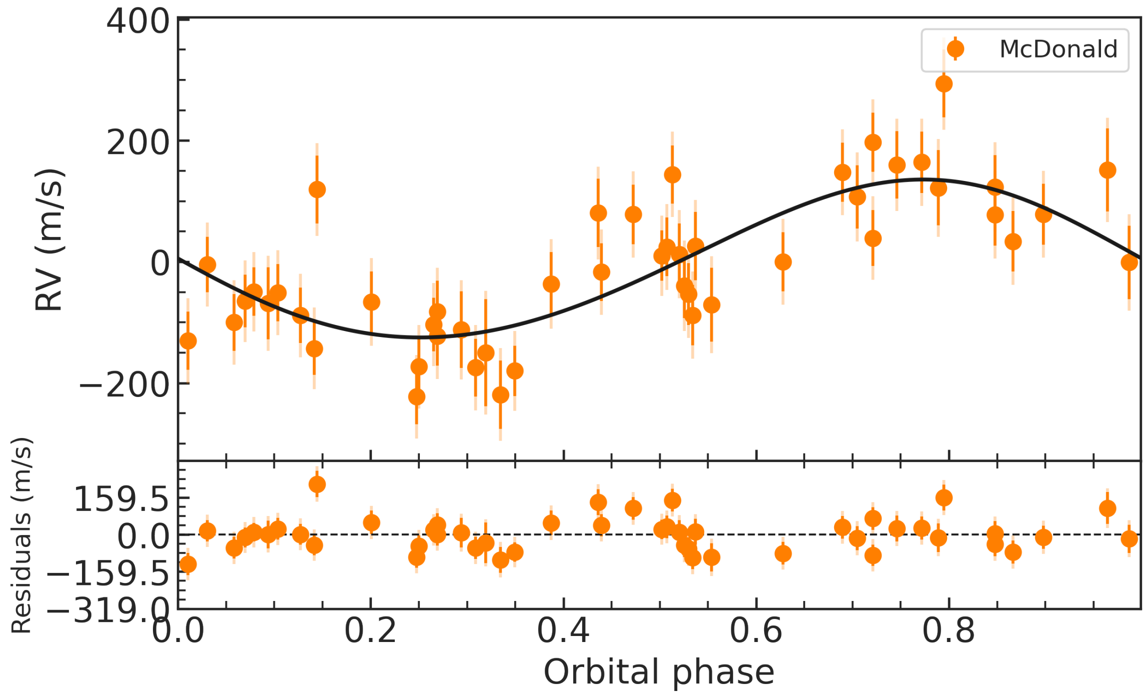

Figure 4. Phase-folded RV curve of TOI-2049 b with the orbital fit.

$0.89 \pm 0.04\,M_\odot$ (isochrones code), and $0.900^{+0.052}_{-0.049}\,M_\odot$ (computed stellar models and machine learning). The adopted stellar parameters obtained are $R_* = 0.89 \pm 0.03\,R_\odot$ and $M_* = 0.90 \pm 0.03\,M_\odot$.

The mass of TOI-4427 b was derived by combining the mass of the star with the RV measurements obtained with the Robert G. Tull spectrometer at the 2.7 m Harlan J. Smith telescope at McDonald Observatory, and the TRES spectrograph at the Tillinghast telescope. The parameters derived for the planet are listed in Table 4, The phase-folded light curve is shown in Figure 8, and the phase-folded RV curve in Figure 9.

3.1.10. TOI-4458 b

TOI-4458 was observed by TESS in Sectors 14, 15, 16, 18, 19, 20, 21, 22, 23, 24, 25, 26, 40, 41, 47, 48, 49, 50, and 51. Using TESS data the orbital period was determined to 3.939 days. TOI-4458 is at the edge, but still in the North PLATO LOP Field (V. Nascimbeni et al. 2022). If PLATO observes this star, the stellar parameters can be determined with a much higher accuracy than before by analyzing stellar oscillations. PLATO will also be able to detect very small transiting planets if there are any.

Speckle observations were obtained with NESSI on the 3.5 m WIYN telescope. These observations exclude companions with $\Delta m \leqslant 5$ mag with separations larger than $0\farcs3$.

Egress and ingress observations of the transit were obtained with the 43 cm telescope at Wendelstein, with the 40 cm telescope at the Observatori Astronómic Albanyá, and with the 1.2 m telescope Keplercam (Figure 10). The estimated PSF of the transit observations is between 1.5 and $7\farcs7$. These observations confirm that the transit is on source. The parameters derived for the host star are given in Table 1. The stellar magnitudes are given in Table 3.

For the stellar radius measurements, we find $2.16^{+0.11}_{-0.07}\,R_\odot$ (ARIADNE), $1.44 \pm 0.09\,R_\odot$ (isochrones code), and $2.046^{+0.045}_{-0.050}\,R_\odot$ (computed stellar models and machine learning). The derived masses are $1.31^{+0.16}_{-0.06}\,M_\odot$ (ARIADNE), $1.44 \pm 0.07\,M_\odot$ (isochrones code), and $1.511^{+0.040}_{-0.051}\,M_\odot$ (computed stellar models and machine learning). The adopted stellar parameters obtained are $R_* = 1.96 \pm 0.04\,R_\odot$ and $M_* = 1.47 \pm 0.04\,M_\odot$.

The mass of TOI-4458 b was derived by combining the mass of the star with the RV measurements obtained with the Robert G. Tull spectrometer at the 2.7 m Harlan J. Smith telescope at McDonald Observatory, the TCES spectrometer on the Alfred–Jensch Telescope, and with FOCES on the Fraunhofer telescope on Mount Wendelstein. The parameters derived for the host star are given in Table 1 and for the planet in Table 4. The phase-folded light curve is shown in Figure 11, and the phase-folded RV curve in Figure 12.

4. Discussion and Conclusions

Despite the detection of more than 1000 HJs, we still do not know how they form. Solving this question is important because HJs are an extreme outcome of planet formation. Thus, a theory of planet formation must explain why they exist.

The various scenarios of their formation make different predictions of their properties. In the high-eccentricity migration scenario, planets are formed at large distances, and then migrate inward via Kozai–Lidov oscillations and/or planet–planet scattering. If either scenario is correct, young HJs should have eccentric orbits. However, depending on the tidal quality factor (Q), the orbits are circularized over time.

The eccentricities of old HJs are thus expected to be small, even if they had large eccentricities when they were young. We have found a significant eccentricity of $0.105^{+0.019}_{-0.019}$ with the MCMC algorithm, and $0.109^{+0.021}_{-0.020}$ with PYANETI, for TOI-2040 b. Because both algorithms give the same results, we conclude that the orbit of TOI-2040 b is slightly eccentric. The eccentricities of the other planets are consistent with circular orbits, with upper limits of the eccentricities between 0.048 and 0.071.

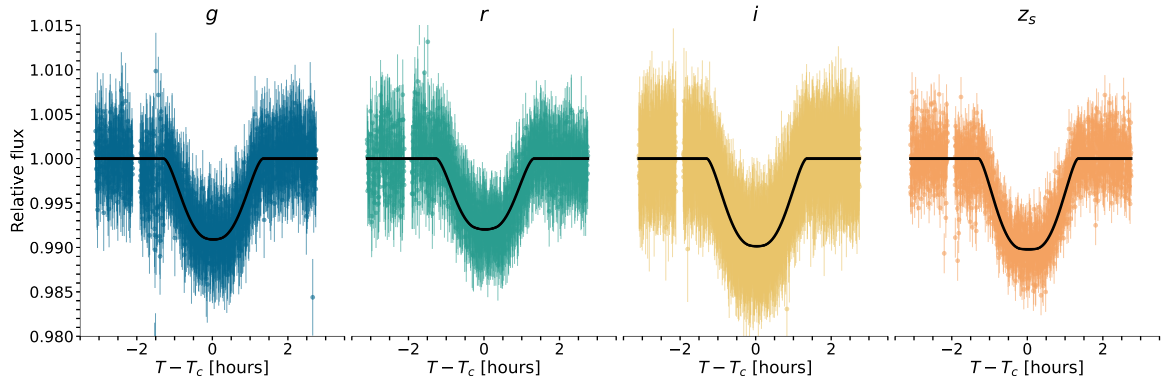

Figure 5. Phase-folded light curve of TOI-2578 in the g,r,i, and zs filters. The systematics were removed. The black lines are fit to the data.

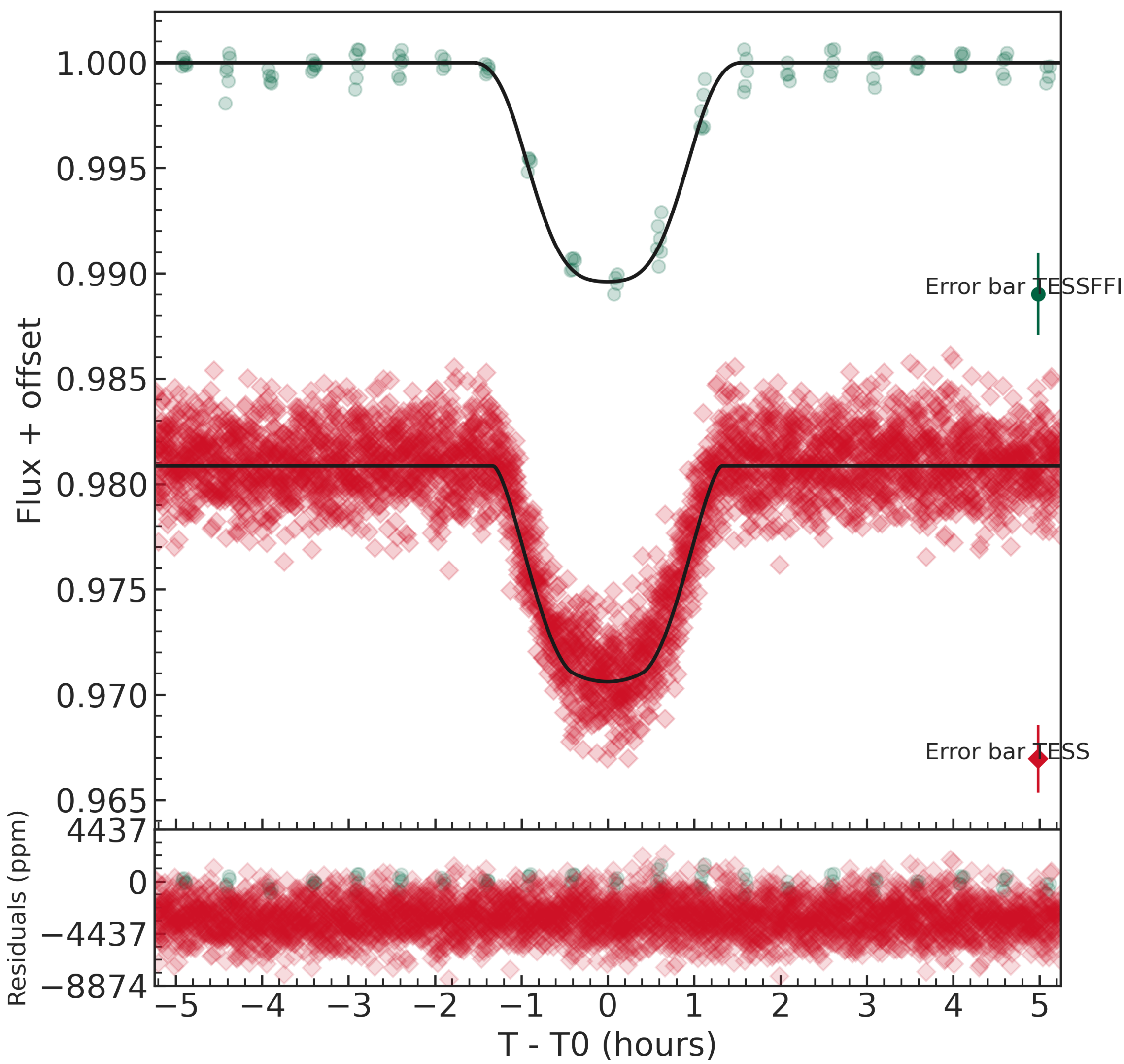

Figure 6. Same as Figure 1 but for TOI-2578.

The detection of a system with an HJ and another planet with an orbital period of less than 100 days would be an argument for in situ formation. On the contrary, the loneliness of HJs is a key argument against in situ formation and in favor of the migration scenario. The five HJs studied in this work shows no sign of additional planets but more observations are needed to put tighter constrains on outer companions, and to improve the eccentricity measurements.

HJs are ideal to study the internal structure of gas-giant planets, because their masses and radii can be determined with relatively high accuracy. Determining the masses, radii, and the ages of planets is one of the key goals of the PLATO mission (H. Rauer et al. 2022), and TOI-4458 b is located in the northern PLATO field. This field will also be observed by the Earth 2.0 Space Mission, which will provide superb photometric data (J. Ge et al. 2024).

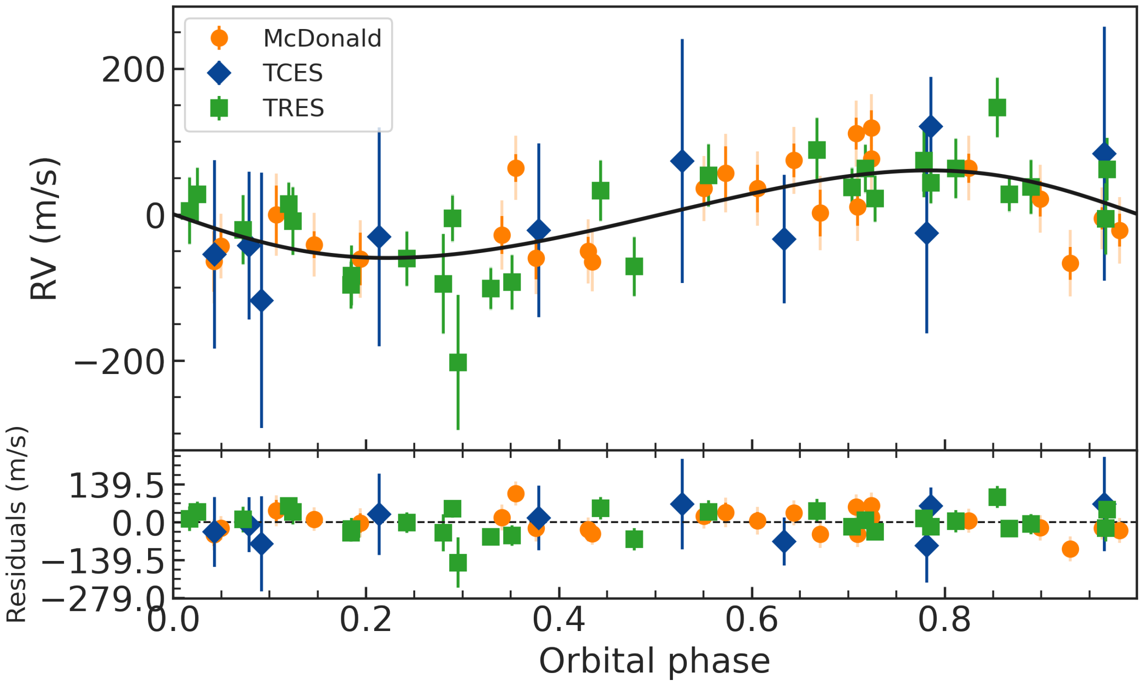

Figure 7. Phase-folded RV curve of TOI-2578 b with the orbital fit.

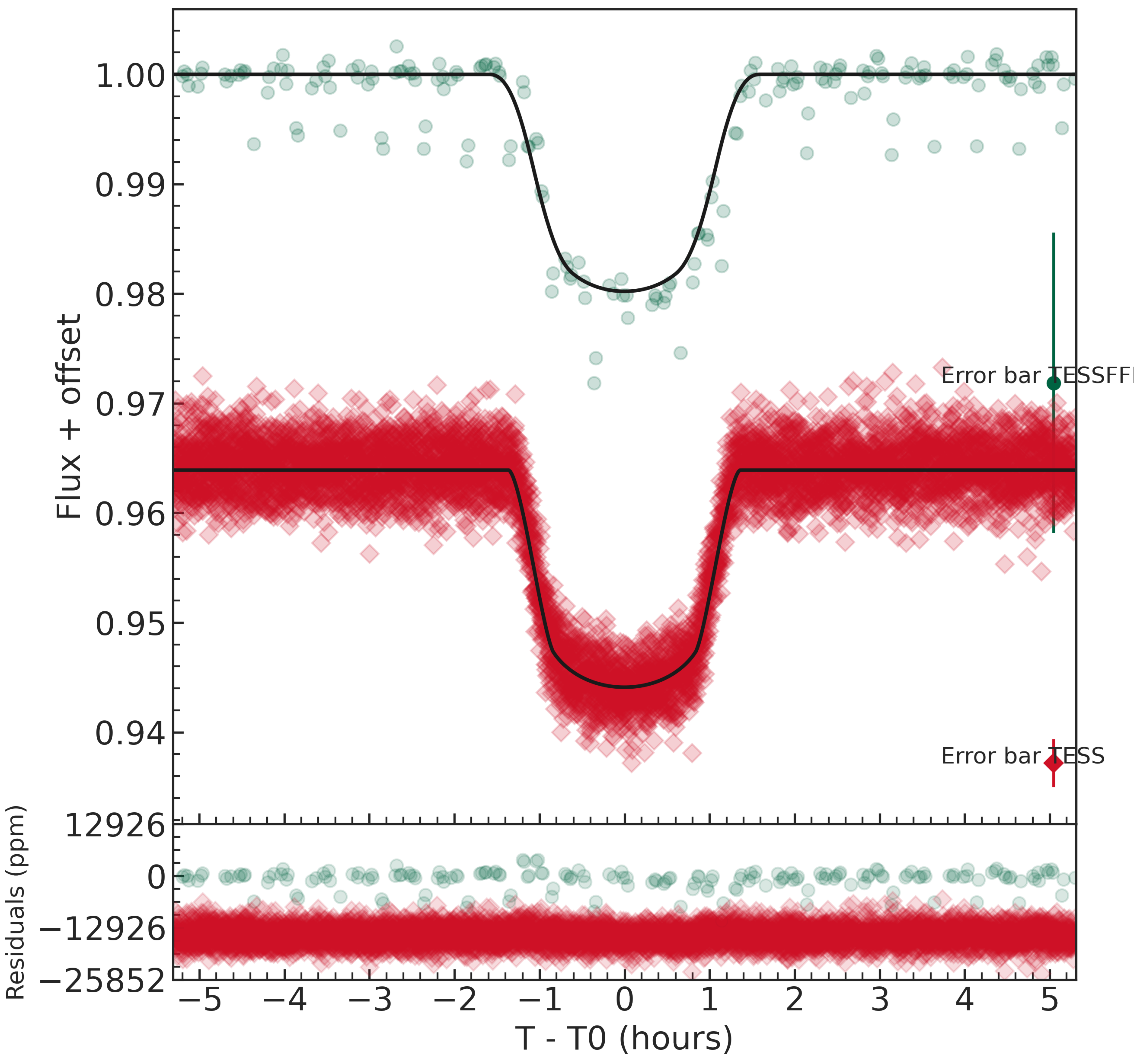

Figure 8. Same as Figure 1 but for TOI-4427.

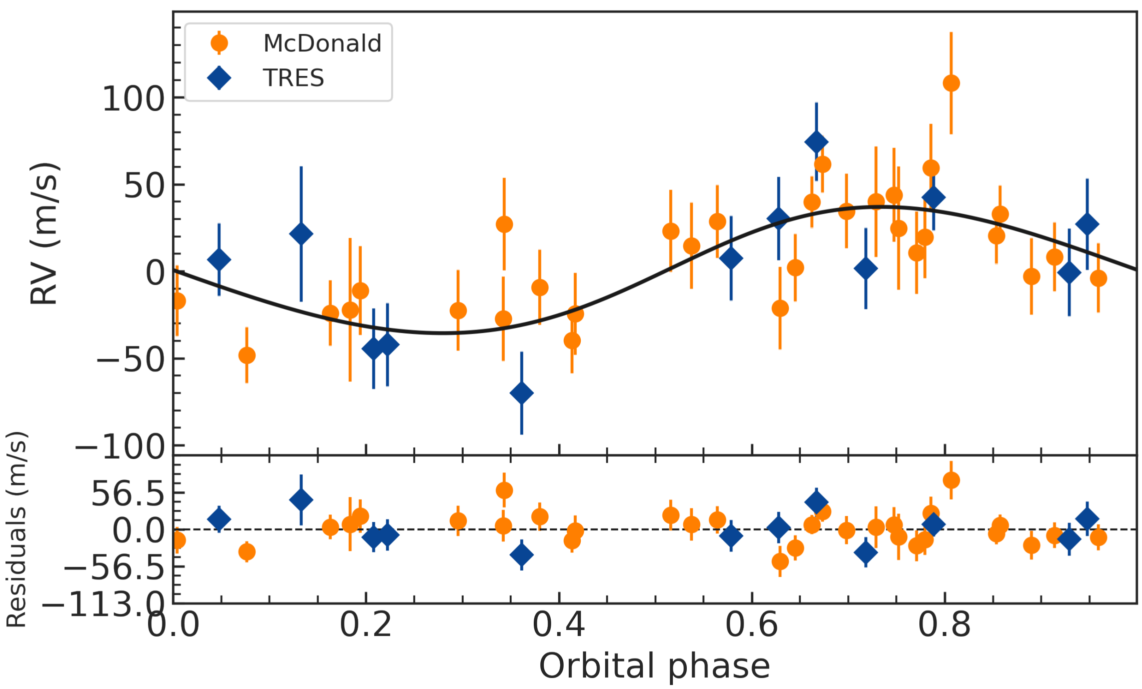

Figure 9. Phase-folded RV curve of TOI-4427 b with the orbital fit.

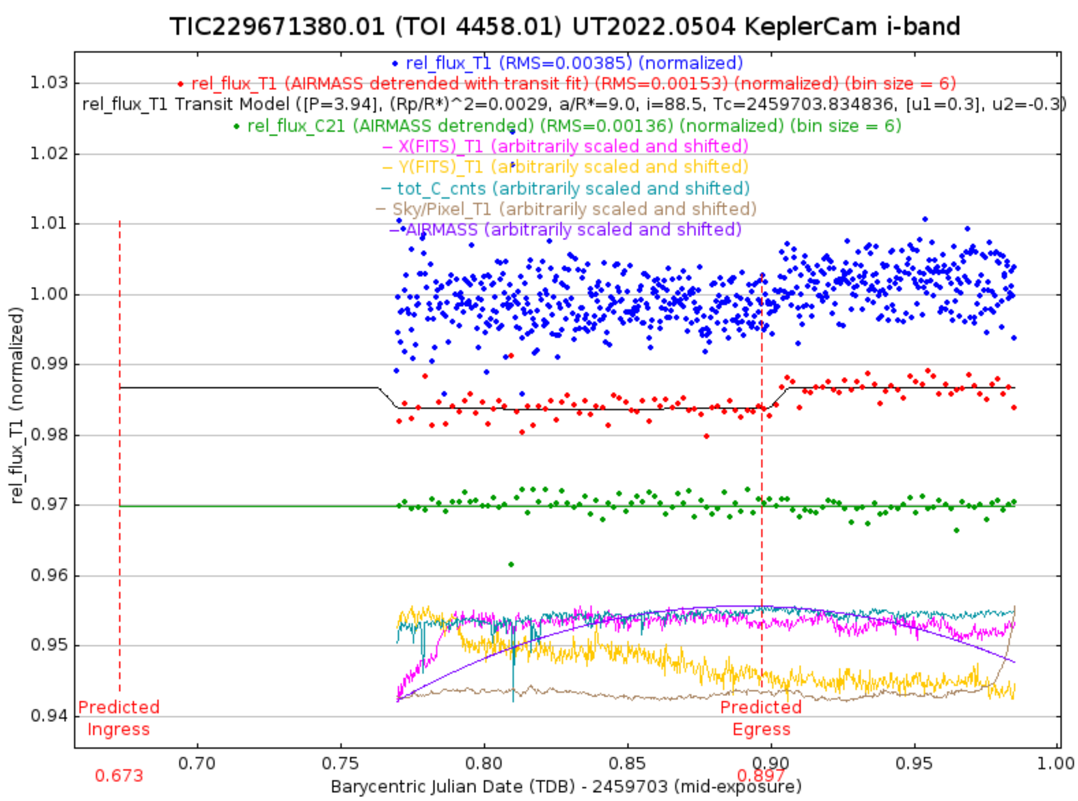

Figure 10. Phase-folded light curve of TOI-4458 obtained with KeplerCam.

Particularly interesting are objects with low density and relatively low temperature. TOI-4427 b has a density of $0.214^{+0.036}_{-0.034}$ g m^{-3}. It is thus a low-density planet but not the planet with the lowest density. For example, WASP-107 b has a density of 0.14 ± 0.02 g m^{-3} (D. R. Anderson et al. 2017), KELT-11 b has $0.093^{+0.028}_{-0.024}$ g m^{-3} (J. Pepper et al. 2017), and WASP-193 b has 0.060 ± 0.019 g m^{-3} (S. W. Yee et al. 2025).

The best targets for atmospheric characterization are gas giants with precise mass, radius, and age determinations that have extended atmospheres and which orbit bright stars (S. Müller & R. Helled 2023). We determined the TSM to

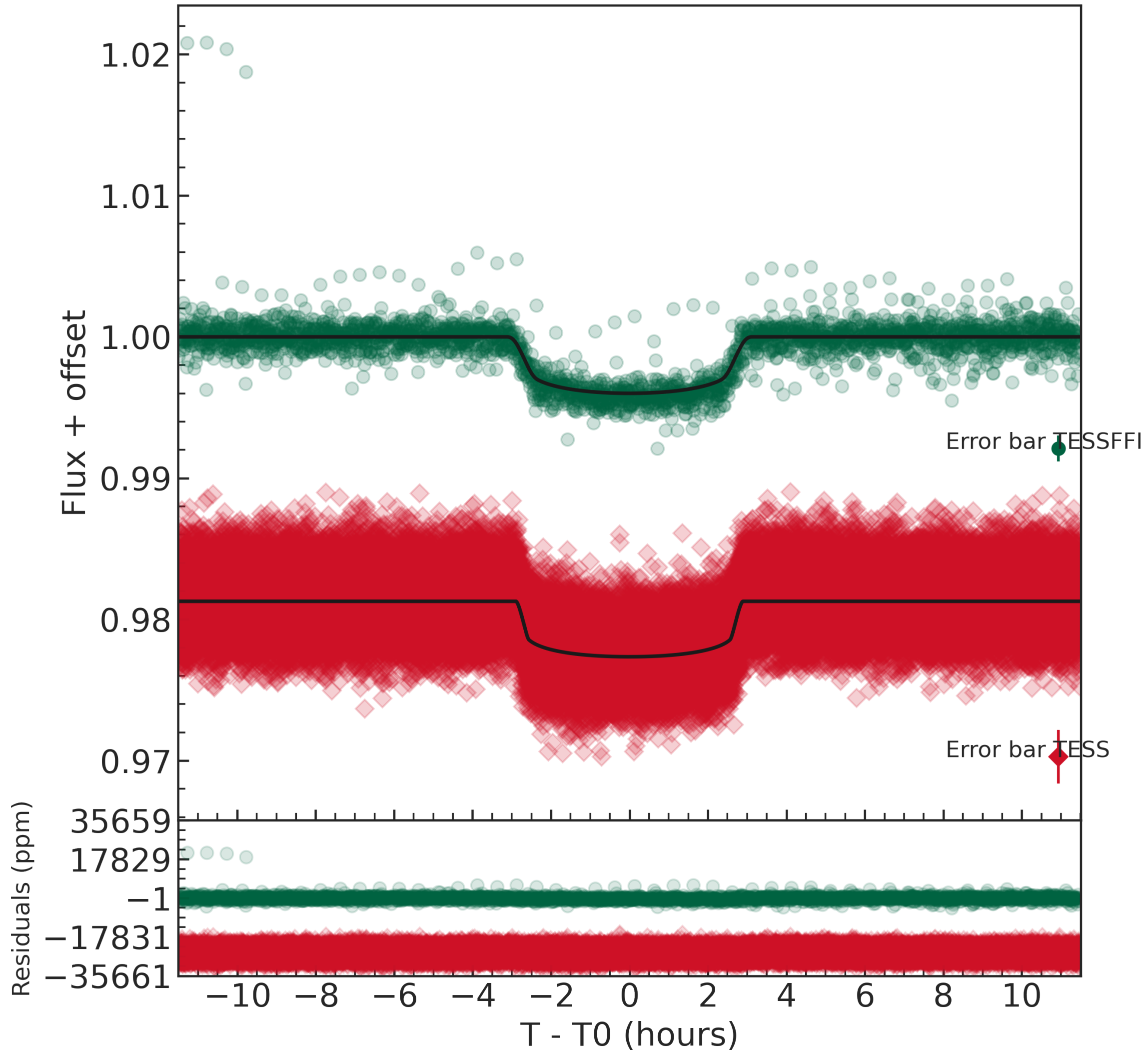

Figure 11. Same as Figure 1 but for TOI-4458.

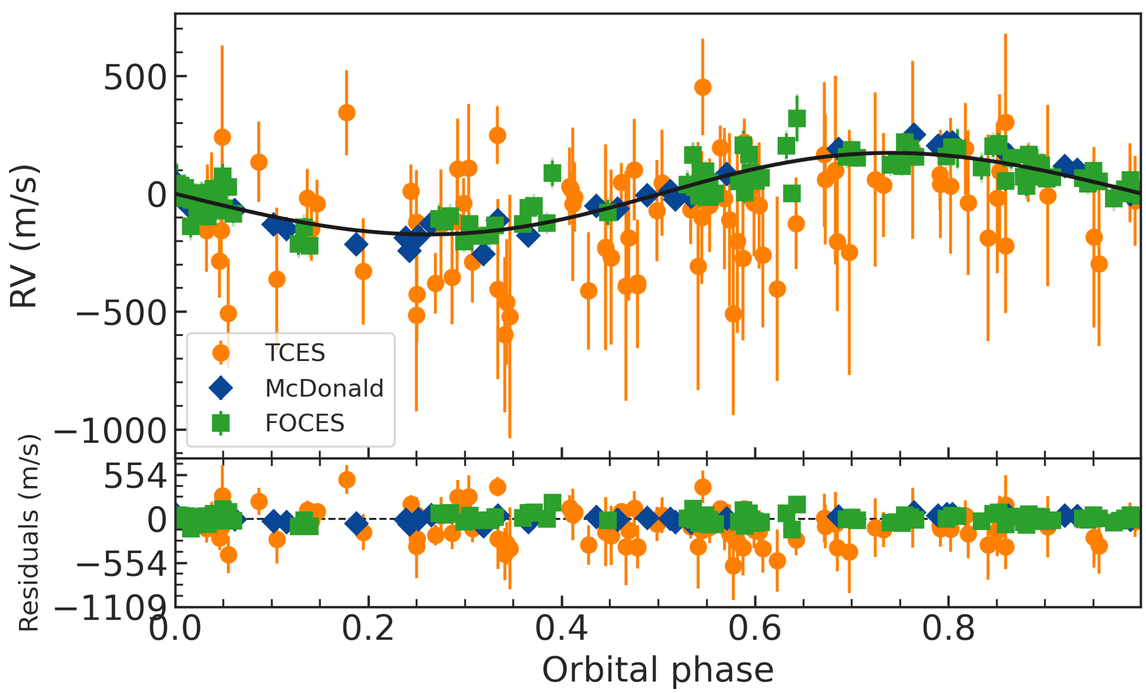

Figure 12. Phase-folded RV curve of TOI-4458 b with the orbital fit.

quantify the expected signal-to-noise ratio in transmission and thermal emission spectroscopy for the planets (E. M. R. Kempton et al. 2018). Because of the inflation of the radii, gas giants with equilibrium temperatures of 1000 K, or less, are preferred over hotter planets. TOI-2040 b and TOI-4427 b have temperatures of about 1000 K. The TSM and T_{eq} values are TSM $= 26.2^{+1.8}_{-1.7}$ and $T_{eq} = 1067^{+29}_{-29}$ K for TOI-2040 b, and TSM $= 147^{28}_{-20}$ and $T_{eq} = 1039^{+46}_{-50}$ K for TOI-4427 b. TOI-2040 b and TOI-4427 b are thus excellent targets for the ARIEL mission (E. Pascale et al. 2018).

Three of the planets studied in this work have temperatures of about 1800 K. We find TSM $= 7.4^{+1.6}_{-1.3}$ and $T_{eq} = 1869^{+128}_{-128}$ K for TOI-2049 b, TSM $= 815^{+135}_{-109}$ and $T_{eq} = 1778^{+75}_{-74}$ K for TOI-2578 b, and TSM $= 6.8^{+0.43}_{-0.39}$ and $T_{eq} = 1759^{+30}_{-31}$ K for TOI-4458 b. These planets are thus also suitable for atmospheric characterization. TOI-2578 b a particularly interesting target because of its low density and large TSM.

Acknowledgments

This paper includes data collected by the TESS mission. Funding for the TESS mission is provided by NASA's Science Mission Directorate. We acknowledge the use of public TOI Release data from pipelines at the TESS Science Office and at the TESS Science Processing Operations Center.

This research has made use of the Exoplanet Follow-up Observation Program (ExoFOP) website with DOI:10.26134/ExoFOP5, which is operated by the California Institute of Technology, under contract with the National Aeronautics and Space Administration under the Exoplanet Exploration Program (NExScI 2022).

This work has made use of data from the European Space Agency (ESA) mission Gaia,[45] processed by the Gaia Data Processing and Analysis Consortium (DPAC).[46] Funding for the DPAC has been provided by national institutions, in particular the institutions participating in the Gaia Multilateral Agreement. The Gaia mission website is https://www.cosmos. esa.int/gaiahttps://www.cosmos.esa.int/gaia. The Gaia archive website is https://archives.esac.esa.int/gaia.

This publication makes use of data products from the Two Micron All Sky Survey, which is a joint project of the University of Massachusetts and the Infrared Processing and Analysis Center/California Institute of Technology, funded by the National Aeronautics and Space Administration and the National Science Foundation

This work has made use of the Mikulski Archive for Space Telescopes (MAST). MAST is a NASA funded project to support and provide to the astronomical community a variety of astronomical data archives, with the primary focus on scientifically related datasets in the optical, ultraviolet, and near-infrared parts of the spectrum.

This research has made use of the SIMBAD database, operated at CDS, Strasbourg, France, and the Encyclopaedia of exoplanetary systems in https://exoplanet.eu.

This work was supported by NASA TESS GI5 Grant 80NSSC23K0429 to The University of Texas at Austin.

E.G. acknowledges the generous support by the Deutsche Forschungsgemeinschaft (DFG) in the framework of the priority program "Exploring the Diversity of Extrasolar Planets" (SPP 1992) in program GU 464/22, and by the Thüringer Ministerium für Bildung, Wissenschaft und Kultur.

B.N. acknowledges postdoctoral funding from the "Branco Weiss fellowship—Science in Society" through the SEISMIC stellar interior physics group. J.K. and B.N. acknowledge funding through the Max-Planck Partnership group—SEISMIC Max-Planck-Institut für Astrophysik (MPA)—Germany and Kyambogo University (KyU)—Uganda. B.N. also acknowledges funding from the UNESCO-TWAS program, "Seed Grant for African Principal Investigators" financed by the German Ministry of Education and Research (BMBF).

This work is partly supported by JSPS KAKENHI grant Nos. JP24H00017, JP24K00689, and JP25K17450, JSPS Bilateral Program Number JPJSBP120249910, JST SPRING, grant No. JPMJSP2108, and JSPS Grant-in-Aid for JSPS Fellows grant No. JP25KJ1036. This article is based on observations made with the MuSCAT2 instrument, developed by ABC, at Telescopio Carlos Sánchez operated on the island of Tenerife by the IAC in the Spanish Observatorio del Teide.

The Wendelstein 2.1 m telescope project was funded by the Bavarian government and by the German Federal government through a common funding process. Part of the 2.1 m instrumentation including some of the upgrades for the infrastructure were funded by the Cluster of Excellence "Origin of the Universe" of the German Science foundation.

P.K. acknowledges the support from ESA PRODEX agreement 4000127913. Mobilities for E.G. and P.K. were funded from EXOWORLD Project ID 101086149D.

D.S.'s research is funded by the European Research Council (ERC) through the European Union's Horizon 2020 research and innovation program (grant agreement n°803193/BEBOP) and by the DLR.

Appendix
Radial-velocity Measurements

The RV measurements obtained are given in Tables 5–9.

[45] https://www.cosmos.esa.int/gaia

[46] https://www.cosmos.esa.int/web/gaia/dpac/consortium

Table 5
Radial-velocity Measurements of TOI-2040

BJD[a] (TDB)[b]	RV (m s^{-1})	Instr.
2459471.777251	15,703.4 ± 17.2	McDonald
2459472.780718	15,877.6 ± 19.0	McDonald
2459515.854723	15,890.9 ± 22.2	McDonald
2459516.713236	15,797.4 ± 17.4	McDonald
2459528.670456	15,736.4 ± 17.1	McDonald
2459529.721264	15,772.7 ± 19.3	McDonald
2459541.698639	15,864.2 ± 17.0	McDonald
2459563.613954	15,702.4 ± 19.7	McDonald
2459593.631080	15,833.2 ± 18.4	McDonald
2459609.606153	15,757.9 ± 21.4	McDonald
2459620.606488	15,855.0 ± 21.4	McDonald
2459621.609846	15,724.6 ± 22.6	McDonald
2459756.902198	15,724.2 ± 20.5	McDonald
2459789.900355	15,935.8 ± 19.0	McDonald
2459790.873859	15,758.3 ± 18.8	McDonald
2459791.898205	15,712.1 ± 17.3	McDonald
2459792.880553	15,841.3 ± 19.9	McDonald
2459797.904671	15,902.6 ± 19.5	McDonald
2459845.782905	15,726.9 ± 19.2	McDonald
2459846.786626	15,812.8 ± 20.4	McDonald
2459847.754641	15,938.3 ± 20.7	McDonald
2459848.751843	15,797.7 ± 21.9	McDonald
2459878.723651	15,854.1 ± 24.0	McDonald
2459906.601738	15,794.1 ± 19.1	McDonald
2459918.586702	15,734.5 ± 23.3	McDonald
2459926.665141	15,712.0 ± 28.9	McDonald
2459956.662687	15,849.5 ± 26.2	McDonald
2459957.613455	15,741.8 ± 23.1	McDonald
2459978.610504	15,955.2 ± 21.9	McDonald
2459979.571661	15,890.0 ± 19.5	McDonald
2459990.587769	15,923.7 ± 29.2	McDonald
2460051.965133	15,921.6 ± 22.1	McDonald
2460162.898155	15,743.7 ± 17.3	McDonald
2460186.914291	15,843.1 ± 17.1	McDonald
2460190.879645	15,900.0 ± 18.5	McDonald
2460193.879772	15,755.6 ± 18.8	McDonald
2460211.812490	15,785.5 ± 35.7	McDonald
2460211.898489	15,732.8 ± 25.2	McDonald
2460212.755857	15,720.1 ± 16.9	McDonald
2460228.758649	15,784.4 ± 16.9	McDonald
2460230.764655	15,795.6 ± 17.1	McDonald
2460231.747503	15,715.4 ± 16.1	McDonald
2460232.765496	15,798.2 ± 19.9	McDonald
2460251.698274	15,739.6 ± 19.6	McDonald
2460252.640361	15,907.8 ± 17.5	McDonald
2460263.782276	15,851.1 ± 20.5	McDonald
2459059.902866	81.56 ± 43.5	TRES[c]
2459173.732645	−199.47 ± 26.1	TRES
2459380.945350	0.00 ± 26.1	TRES
2459381.943885	−162.64 ± 24.4	TRES
2459395.935143	37.11 ± 25.1	TRES

[a] Barycentric Julian date (BJD)
[b] Barycentric dynamical time (TDB).
[c] Velocity relative to the template of that instrument.

Table 6
Radial-velocity Measurements of TOI-2578

BJD (TDB)	RV (m s^{-1})	Instr.
2459302.636390	36,551.62 ± 22.65	McDonald
2459308.655190	36,620.56 ± 31.89	McDonald
2459454.964460	36,596.91 ± 22.49	McDonald
2459515.909359	36,654.06 ± 32.31	McDonald
2459528.946392	36,558.82 ± 29.31	McDonald
2459591.791746	36,654.04 ± 20.24	McDonald
2459592.741502	36,682.12 ± 19.89	McDonald

Table 6
(Continued)

BJD (TDB)	RV (m s^{-1})	Instr.
2459593.717256	36,618.18 ± 40.03	McDonald
2459609.633802	36,629.18 ± 25.86	McDonald
2459610.784735	36,554.10 ± 41.68	McDonald
2459620.661426	36,640.09 ± 24.19	McDonald
2459621.682488	36,557.60 ± 35.83	McDonald
2459633.610585	36,692.70 ± 23.0	McDonald
2459634.715383	36,613.40 ± 15.1	McDonald
2459790.957622	36,577.20 ± 18.3	McDonald
2459791.954423	36,554.00 ± 10.5	McDonald
2459792.954415	36,694.70 ± 18.6	McDonald
2459845.951321	36,575.50 ± 19.9	McDonald
2459846.957084	36,590.40 ± 25.8	McDonald
2459878.880739	36,675.40 ± 36.4	McDonald
2459927.760369	36,729.50 ± 21.9	McDonald
2459957.663048	36,682.40 ± 18.9	McDonald
2459978.668883	36,568.00 ± 19.8	McDonald
2459979.685390	36,737.10 ± 24.3	McDonald
2456670.598900	−21.1 ± 49.6	TRES[a]
2456675.661473	−155.3 ± 37.1	TRES
2456677.629855	−31.7 ± 40.7	TRES
2459604.723283	−100.0 ± 31.3	TRES
2459605.641213	−41.1 ± 42.4	TRES
2459606.676039	51.8 ± 40.4	TRES
2459607.594314	−80.3 ± 28.7	TRES
2459608.711776	−62.0 ± 41.3	TRES
2459609.661865	−31.8 ± 32.4	TRES
2459610.724746	−67.4 ± 36.6	TRES
2459611.605336	−189.8 ± 68.0	TRES
2459611.658943	−297.4 ± 92.6	TRES
2459611.775850	−196.2 ± 27.8	TRES
2459613.712651	−56.9 ± 36.8	TRES
2459614.735334	−178.2 ± 40.6	TRES
2459616.612570	−73.1 ± 31.1	TRES
2459617.612614	−89.6 ± 45.2	TRES
2459618.768102	−187.5 ± 37.1	TRES
2459958.741730	−6.6 ± 43.8	TRES
2459963.601567	−115.6 ± 47.1	TRES
2459969.805397	−67.1 ± 22.5	TRES
2459970.694915	−103.6 ± 46.2	TRES
2459972.700217	−57.8 ± 26.0	TRES
2459973.613429	−32.7 ± 42.6	TRES
2460270.995072	−100.7 ± 48.9	TRES
2460271.745985	−191.2 ± 32.0	TRES
2460272.761665	−166.1 ± 40.4	TRES
2460273.824786	−51.1 ± 27.8	TRES
2459980.520963	423 ± 174	TCES[a]
2459981.378683	309 ± 150	TCES
2459984.246136	285 ± 129	TCES
2459984.415245	222 ± 175	TCES
2459985.408648	318 ± 119	TCES
2459986.287965	306 ± 88	TCES
2459989.381194	413 ± 167	TCES
2459990.257745	314 ± 137	TCES
2459990.272548	460 ± 68	TCES
2459991.286194	297 ± 101	TCES

Note.
[a] Velocity relative to the template of that instrument.

Table 7
Radial-velocity Measurements of TOI-2049

BJD (TDB)	RV (m s^{-1})	Instr.
2459454.847786	−35,783.8 ± 41.3	McDonald
2459455.802994	−35,657.0 ± 50.9	McDonald
2459471.736520	−35,691.9 ± 49.8	McDonald
2459472.728790	−35,564.6 ± 45.8	McDonald
2459515.828784	−35,480.5 ± 52.9	McDonald

Table 7
(Continued)

BJD (TDB)	RV (m s^{-1})	Instr.
2459516.689479	−35,734.1 ± 48.0	McDonald
2459528.648188	−35,707.3 ± 44.5	McDonald
2459529.746765	−35,525.5 ± 49.1	McDonald
2459541.674091	−35,406.4 ± 48.6	McDonald
2459563.656982	−35,569.9 ± 49.6	McDonald
2459592.657462	−35,822.8 ± 56.4	McDonald
2459593.605187	−35,459.6 ± 48.0	McDonald
2459609.581021	−35,643.2 ± 53.7	McDonald
2459621.585357	−35,481.6 ± 61.9	McDonald
2459693.961304	−35,523.2 ± 56.5	McDonald
2459749.919867	−35,604.6 ± 60.5	McDonald
2459752.924947	−35,674.8 ± 61.0	McDonald
2459753.944239	−35,443.9 ± 55.7	McDonald
2459756.928323	−35,778.5 ± 47.5	McDonald
2459767.952335	−35,640.4 ± 52.8	McDonald
2459789.871828	−35,591.4 ± 51.1	McDonald
2459790.850652	−35,496.7 ± 52.5	McDonald
2459791.875467	−35,525.3 ± 50.0	McDonald
2459792.910626	−35,672.3 ± 59.2	McDonald
2459797.881579	−35,608.3 ± 45.7	McDonald
2459845.759938	−35,703.8 ± 46.7	McDonald
2459846.764296	−35,826.3 ± 45.7	McDonald
2459847.779252	−35,620.8 ± 47.4	McDonald
2459848.778453	−35,603.7 ± 48.7	McDonald
2459878.697534	−35,686.2 ± 51.1	McDonald
2459906.636656	−35,577.7 ± 56.2	McDonald
2459918.609674	−35,309.5 ± 55.9	McDonald
2459926.696860	−35,753.9 ± 88.2	McDonald
2459956.633956	−35,452.3 ± 68.5	McDonald
2459957.588101	−35,484.5 ± 56.2	McDonald
2459978.586918	−35,655.0 ± 47.1	McDonald
2459979.595312	−35,715.8 ± 63.3	McDonald
2460052.958169	−35,692.3 ± 45.7	McDonald
2460123.892154	−35,593.8 ± 41.5	McDonald
2460124.886430	−35,455.9 ± 48.5	McDonald
2460142.862325	−35,653.1 ± 40.0	McDonald
2460162.850261	−35,526.1 ± 51.0	McDonald
2460185.935607	−35,670.2 ± 50.6	McDonald
2460188.965416	−35,439.6 ± 50.5	McDonald
2460190.924710	−35,746.8 ± 43.3	McDonald
2460192.865967	−35,579.3 ± 48.4	McDonald
2460211.759934	−35,668.6 ± 43.3	McDonald
2460212.714864	−35,776.8 ± 45.3	McDonald
2460228.728251	−35,726.4 ± 48.4	McDonald

Note.
[a] Velocity relative to the template.

Table 8
Radial-velocity Measurements of TOI-4427

BJD (TDB)	RV (m s^{-1})	Instr.
2459609.875903	−48,597.7 ± 23.4	McDonald
2459610.854623	−48,594.5 ± 23.6	McDonald
2459620.814117	−48,513.7 ± 25.1	McDonald
2459621.823442	−48,590.1 ± 20.2	McDonald
2459634.765477	−48,465.0 ± 29.3	McDonald
2459692.659623	−48,600.6 ± 24.1	McDonald
2459693.684084	−48,544.6 ± 20.8	McDonald
2459694.678213	−48,553.5 ± 23.6	McDonald
2459705.684789	−48,597.3 ± 18.7	McDonald
2459706.689406	−48,582.4 ± 21.5	McDonald
2459756.630648	−48,584.3 ± 25.4	McDonald
2459757.643876	−48,613.1 ± 18.6	McDonald
2459906.001012	−48,558.5 ± 24.7	McDonald
2459906.969949	−48,529.3 ± 26.9	McDonald
2459957.879228	−48,562.6 ± 23.5	McDonald
2459978.774994	−48,595.7 ± 23.1	McDonald
2459979.793907	−48,550.0 ± 23.5	McDonald
2459992.849708	−48,546.1 ± 26.5	McDonald
2460003.726862	−48,538.6 ± 21.3	McDonald
2460017.722426	−48,533.2 ± 31.7	McDonald
2460017.830532	−48,548.4 ± 35.3	McDonald
2460018.786824	−48,577.1 ± 19.8	McDonald
2460033.677956	−48,595.4 ± 41.2	McDonald
2460050.644930	−48,540.4 ± 16.4	McDonald
2460051.655306	−48,621.5 ± 15.9	McDonald
2460064.759242	−48,565.0 ± 19.7	McDonald
2460086.689287	−48,533.5 ± 14.6	McDonald
2460109.700442	−48,571.2 ± 19.3	McDonald
2460110.663965	−48,552.7 ± 16.1	McDonald
2460289.942342	−48,511.7 ± 16.1	McDonald
2460290.943721	−48,576.2 ± 21.9	McDonald
2459546.934712	−9.9 ± 18.8	TRES[a]
2459548.939090	−94.7 ± 23.8	TRES
2459608.908637	−97.0 ± 23.0	TRES
2459610.849547	−22.1 ± 23.8	TRES
2459615.885381	−50.9 ± 23.2	TRES
2459616.858411	−53.1 ± 25.1	TRES
2459617.799496	−31.0 ± 38.8	TRES
2459618.856276	−122.5 ± 23.7	TRES
2459619.858596	−45.0 ± 24.2	TRES
2459624.883843	22.0 ± 22.5	TRES
2459630.798680	−25.4 ± 26.2	TRES
2459635.878306	−45.8 ± 20.7	TRES

Note.
[a] Velocity relative to the template.

Table 9
Radial-velocity Measurements of TOI-4458

BJD (TDB)	RV (m s^{-1})	Instr.
2459480.393705	432 ± 213	TCES[a]
2459480.592826	−133 ± 266	TCES
2459503.578474	671 ± 180	TCES
2459593.612491	172 ± 175	TCES
2459593.634273	329 ± 172	TCES
2459593.665060	41 ± 154	TCES
2459600.644528	518 ± 194	TCES
2459658.363474	140 ± 265	TCES
2459658.385824	429 ± 215	TCES
2459660.404551	374 ± 167	TCES
2459660.426368	297 ± 190	TCES
2459661.415396	338 ± 111	TCES
2459661.437178	207 ± 220	TCES
2459661.629076	286 ± 106	TCES
2459661.650870	437 ± 270	TCES
2459662.417097	256 ± 214	TCES
2459662.438845	374 ± 224	TCES
2459662.631576	278 ± 197	TCES
2459679.561379	309 ± 319	TCES
2459679.595002	631 ± 374	TCES
2459681.494412	−271 ± 329	TCES
2459681.515361	−194 ± 516	TCES
2459682.425442	−182 ± 430	TCES
2459683.462386	140 ± 438	TCES
2459686.448648	287 ± 223	TCES
2459686.470442	277 ± 267	TCES
2459687.449897	422 ± 327	TCES
2459688.443787	−35 ± 303	TCES
2459709.481160	94 ± 430	TCES
2459709.503116	56 ± 369	TCES
2459713.550268	−51 ± 268	TCES
2459714.356599	425 ± 397	TCES
2459745.419690	306 ± 299	TCES
2459745.440639	217 ± 367	TCES
2459746.411391	289 ± 307	TCES
2459748.436090	−78 ± 382	TCES
2459749.412051	125 ± 388	TCES
2459749.433833	54 ± 348	TCES
2459753.454724	67 ± 306	TCES
2459754.444007	106 ± 285	TCES
2459757.451854	−77 ± 391	TCES
2459769.514829	124 ± 294	TCES
2459772.440581	−85 ± 248	TCES
2459779.401785	−2 ± 225	TCES
2459795.521761	−28 ± 198	TCES
2459799.392664	−53 ± 128	TCES
2459799.544458	37 ± 171	TCES
2459800.433671	260 ± 145	TCES
2459801.447653	409 ± 151	TCES[a]
2459802.459493	172 ± 146	TCES
2459824.337213	418 ± 94	TCES
2459826.463601	176 ± 133	TCES
2459826.486067	285 ± 100	TCES
2459829.383995	415 ± 122	TCES
2459831.453729	358 ± 164	TCES
2459831.475685	313 ± 146	TCES
2459834.326032	309 ± 122	TCES
2459835.399933	348 ± 68	TCES
2459835.604863	375 ± 80	TCES
2459709.481160	100 ± 436	TCES
2459709.503116	58 ± 371	TCES
2459713.550268	−62 ± 266	TCES
2459714.356599	427 ± 400	TCES

Table 9
(Continued)

BJD (TDB)	RV (m s^{-1})	Instr.
2459715.409273	143 ± 382	TCES
2459715.431113	30 ± 349	TCES
2459717.441715	−64 ± 487	TCES
2459718.351981	78 ± 520	TCES
2459722.550430	513 ± 377	TCES
2459980.627294	194 ± 235	TCES
2459984.469423	−100 ± 201	TCES
2459984.633000	209 ± 234	TCES
2459986.335835	387 ± 370	TCES
2459989.553555	20 ± 526	TCES
2459989.568937	226 ± 281	TCES
2459990.541368	368 ± 229	TCES
2459991.553254	567 ± 389	TCES
2459991.578185	−181 ± 232	TCES
2460108.491009	364 ± 220	TCES
2460110.527329	−189 ± 407	TCES
2460124.521692	360 ± 288	TCES
2460155.405859	201 ± 193	TCES
2460186.542155	780 ± 204	TCES
2460192.403081	337 ± 112	TCES
2460192.610454	462 ± 170	TCES
2460193.583324	576 ± 122	TCES
2460194.492525	522 ± 92	TCES
2460194.589782	547 ± 97	TCES
2460089.463150	319 ± 384	TCES
2460091.466866	282 ± 325	TCES
2460092.491750	493 ± 307	TCES
2460096.434065	388 ± 275	TCES
2459609.981365	5253.8 ± 34.3	McDonald
2459610.958905	5417.8 ± 36.5	McDonald
2459621.012530	5466.8 ± 33.0	McDonald
2459622.000953	5283.0 ± 39.4	McDonald
2459609.981365	5253.8 ± 34.3	McDonald
2459610.958905	5417.8 ± 36.5	McDonald
2459621.012530	5466.8 ± 33.0	McDonald
2459622.000953	5283.0 ± 39.4	McDonald
2459634.917120	5445.7 ± 39.7	McDonald
2459692.923440	5227.0 ± 31.7	McDonald
2459693.892894	5462.3 ± 23.1	McDonald
2459705.889104	5456.7 ± 23.7	McDonald
2459706.896816	5672.2 ± 29.3	McDonald
2459706.955216	5686.1 ± 33.5	McDonald
2459707.856656	5423.9 ± 26.1	McDonald
2459750.745691	5586.3 ± 35.0	McDonald
2459753.762697	5660.0 ± 30.1	McDonald
2459754.736390	5571.1 ± 29.0	McDonald
2459756.802753	5405.6 ± 27.6	McDonald
2459789.659615	5685.9 ± 28.3	McDonald
2459790.695884	5399.9 ± 27.3	McDonald
2459791.710359	5214.0 ± 30.3	McDonald
2459792.700428	5552.8 ± 31.9	McDonald
2459797.788602	5634.4 ± 37.2	McDonald
2459798.733408	5339.7 ± 31.3	McDonald
2459799.647309	5355.7 ± 29.7	McDonald
2459845.609701	5515.5 ± 33.1	McDonald
2459846.595837	5287.9 ± 32.6	McDonald
2459847.623364	5479.6 ± 31.6	McDonald
2459848.614815	5720.1 ± 29.1	McDonald
2460018.991462	5420.1 ± 32.7	McDonald
2460019.981224	5343.0 ± 34.7	McDonald
2460050.906495	5318.7 ± 41.7	McDonald
2460051.892150	5290.9 ± 26.5	McDonald
2459741.5379861	49.7 ± 30.7	FOCES[a]

Table 9
(Continued)

BJD (TDB)	RV (m s^{-1})	Instr.
2459741.5626620	3.1 ± 44.9	FOCES
2459777.4310069	154.8 ± 28.0	FOCES
2459777.4530093	183.2 ± 31.8	FOCES
2459777.4750000	150.0 ± 18.1	FOCES
2459785.4903009	121.2 ± 28.4	FOCES
2459785.5152893	127.5 ± 22.4	FOCES
2459785.5372917	115.2 ± 21.4	FOCES
2459794.4010764	40.5 ± 82.8	FOCES
2459794.4341551	23.4 ± 45.1	FOCES
2459794.4570370	−140.8 ± 46.0	FOCES
2459794.4794097	−14.8 ± 41.1	FOCES
2459794.5015509	−20.6 ± 60.2	FOCES
2459794.5248148	−43.8 ± 36.6	FOCES
2459794.5477894	−66.2 ± 20.1	FOCES
2459794.5698264	−73.4 ± 26.5	FOCES
2459794.5920949	−64.4 ± 33.2	FOCES
2459799.5771644	−182.5 ± 23.6	FOCES
2459800.4197106	36.5 ± 48.6	FOCES
2459800.4417130	161.4 ± 39.3	FOCES[a]
2459821.3704398	108.1 ± 20.0	FOCES
2459821.3924769	104.2 ± 15.3	FOCES
2459821.4144907	143.9 ± 19.7	FOCES
2459824.3799074	−28.2 ± 90.6	FOCES
2459824.4019213	18.7 ± 32.4	FOCES
2459826.4558565	−106.5 ± 28.9	FOCES
2459826.4778356	−176.3 ± 19.1	FOCES
2459826.4998148	−160.2 ± 20.8	FOCES
2459827.4545255	−175.0 ± 40.6	FOCES
2459827.4765046	−152.7 ± 44.6	FOCES
2459827.4984838	−70.2 ± 34.9	FOCES
2459834.5532407	−224.8 ± 49.4	FOCES
2459834.5751736	−157.8 ± 57.9	FOCES
2459835.4650579	−146.0 ± 51.2	FOCES
2459835.4871181	10.3 ± 39.8	FOCES
2459857.2875810	139.0 ± 48.2	FOCES
2459857.3095602	3.0 ± 41.0	FOCES
2459857.3315046	16.7 ± 30.9	FOCES
2459857.3534491	16.2 ± 33.0	FOCES
2459857.3753935	55.6 ± 33.6	FOCES
2459857.3973495	15.2 ± 37.6	FOCES
2459857.4192940	−10.8 ± 30.7	FOCES
2459857.4412384	−20.2 ± 28.3	FOCES
2459857.4631829	−3.7 ± 23.9	FOCES
2459857.4851389	−17.8 ± 20.3	FOCES
2459857.5070833	0.1 ± 22.6	FOCES
2459857.5296759	−2.5 ± 32.0	FOCES
2459857.5516319	0.4 ± 37.1	FOCES
2459857.5735764	−23.5 ± 30.5	FOCES
2459857.5955093	−29.2 ± 37.2	FOCES
2459857.6174537	71.8 ± 53.2	FOCES
2459857.6393981	26.8 ± 38.5	FOCES
2459857.6613426	−87.1 ± 40.3	FOCES
2459859.5409490	25.9 ± 32.1	FOCES
2459859.5628819	86.8 ± 38.4	FOCES
2459859.5848380	93.9 ± 24.6	FOCES
2459860.3964120	217.5 ± 26.1	FOCES
2459860.4183565	188.8 ± 24.4	FOCES
2459860.4403009	153.9 ± 17.6	FOCES
2459862.4388889	−108.3 ± 54.1	FOCES
2459862.4608449	−121.8 ± 46.9	FOCES
2459862.4828125	−97.3 ± 34.2	FOCES
2459870.4194560	−205.0 ± 29.2	FOCES
2459870.4416088	−130.3 ± 26.0	FOCES
2459872.3841088	155.4 ± 33.7	FOCES
2459872.4062616	195.1 ± 41.2	FOCES
2459872.4286921	189.6 ± 80.5	FOCES
2459878.4026852	−178.8 ± 38.6	FOCES
2459878.4246644	−135.8 ± 23.2	FOCES
2459879.4361574	202.7 ± 61.3	FOCES
2459879.4581366	163.3 ± 29.0	FOCES
2459879.4801042	73.3 ± 28.7	FOCES
2459883.4033565	87.7 ± 38.3	FOCES
2459883.4253704	51.6 ± 33.2	FOCES
2459883.4473611	65.7 ± 37.6	FOCES
2459884.3450000	109.0 ± 51.5	FOCES
2459884.3929630	199.8 ± 45.0	FOCES
2459884.4149884	210.0 ± 44.7	FOCES
2459886.4160185	−129.9 ± 29.2	FOCES
2459886.4379977	−62.3 ± 30.2	FOCES
2459886.4599769	−54.2 ± 33.9	FOCES
2459888.4554861	69.3 ± 31.6	FOCES
2459888.4774653	164.2 ± 37.0	FOCES
2459888.4994444	70.3 ± 38.3	FOCES
2459890.7023495	−81.7 ± 52.8	FOCES
2459891.4286690	200.4 ± 53.4	FOCES
2459891.4506944	−0.1 ± 3.3	FOCES
2459891.4727083	317.5 ± 95.8	FOCES
2459892.6357870	63.5 ± 26.3	FOCES
2459892.6577662	40.3 ± 26.9	FOCES
2459892.6797454	94.7 ± 38.3	FOCES
2459892.7017361	49.6 ± 25.2	FOCES
2459894.3922569	−127.4 ± 25.5	FOCES
2459894.4142361	84.6 ± 53.8	FOCES
2459900.3464931	119.0 ± 37.6	FOCES
2459900.3684606	62.6 ± 34.4	FOCES
2459900.3904398	67.5 ± 26.3	FOCES
2459926.5490741	−9.3 ± 43.0	FOCES
2459926.5710764	−17.5 ± 47.3	FOCES
2459926.5930556	−1.9 ± 56.6	FOCES
2459931.7156134	51.8 ± 41.0	FOCES
2459931.7375579	150.4 ± 45.7	FOCES
2459946.2231019	−11.7 ± 48.8	FOCES
2459946.2450810	53.5 ± 56.7	FOCES
2459946.2670486	44.6 ± 23.0	FOCES
2459952.4717708	−215.6 ± 46.1	FOCES
2459952.4937847	−143.8 ± 39.2	FOCES
2459952.5157986	−223.5 ± 33.6	FOCES
2459955.4369097	30.5 ± 42.8	FOCES
2459955.4588889	104.9 ± 37.0	FOCES
2459955.4808565	127.9 ± 57.2	FOCES
2459991.2475347	−23.3 ± 36.2	FOCES
2459991.2723727	−1.5 ± 29.2	FOCES
2459991.2943403	17.1 ± 38.0	FOCES
2459991.3185880	1.3 ± 24.6	FOCES
2459991.3405671	−2.3 ± 22.7	FOCES
2459991.3625347	−14.7 ± 24.6	FOCES
2459991.3845023	31.7 ± 20.2	FOCES
2459991.4064815	−9.4 ± 18.9	FOCES
2459991.4304630	−29.3 ± 53.0	FOCES
2459991.4524421	−99.1 ± 41.8	FOCES
2459991.4744213	−61.6 ± 31.3	FOCES
2459991.4963889	−100.2 ± 25.2	FOCES
2459991.5183565	19.5 ± 39.1	FOCES
2459991.5403356	−39.7 ± 44.3	FOCES

Note.
[a] Velocity relative to the template.

ORCID iDs

Eike W. Guenther https://orcid.org/0000-0002-9130-6747
William D. Cochran https://orcid.org/0000-0001-9662-3496
Phillip J. MacQueen https://orcid.org/0009-0006-7054-0100
Elisa Goffo https://orcid.org/0000-0001-9670-961X
Hanna Kellermann https://orcid.org/0009-0006-3527-0424
Benard Nsamba https://orcid.org/0000-0001-7520-0005
Michael Endl https://orcid.org/0000-0002-7714-6310
Daniel Sebastian https://orcid.org/0000-0002-2214-9258
Davide Gandolfi https://orcid.org/0000-0001-8627-9628
Oscar Barragán https://orcid.org/0000-0003-0563-0493
Slawomir Bednarz https://orcid.org/0009-0000-1171-3370
Krzysztof Bernacki https://orcid.org/0000-0003-4647-7114
Allyson Bieryla https://orcid.org/0000-0001-6637-5401
Pau Bosch-Cabot https://orcid.org/0000-0002-1514-5558
Ilaria Carleo https://orcid.org/0000-0002-0810-3747
David R. Ciardi https://orcid.org/0000-0002-5741-3047
Clark Catherine A. Clark https://orcid.org/0000-0002-2361-5812
Szilard Csizmadia https://orcid.org/0000-0001-6803-9698
Hans J. Deeg https://orcid.org/0000-0003-0047-4241
Juliana Ehrhardt https://orcid.org/0009-0003-9433-043X
Mark E. Everett https://orcid.org/0000-0002-0885-7215
Malcolm Fridlund https://orcid.org/0000-0002-0855-8426
Akihiko Fukui https://orcid.org/0000-0002-4909-5763
Iskra Georgieva https://orcid.org/0000-0002-5056-1899
Teruyuki Hirano https://orcid.org/0000-0003-3618-7535
Petr Kabáth https://orcid.org/0000-0002-1623-5352
Juma Kamulali https://orcid.org/0009-0005-5492-8482
Yugo Kawai https://orcid.org/0000-0002-0488-6297
John Kielkopf https://orcid.org/0000-0003-0497-2651
Judith Korth https://orcid.org/0000-0002-0076-6239
David. W. Latham https://orcid.org/0000-0001-9911-7388
John H. Livingston https://orcid.org/0000-0002-4881-3620
Michael B. Lund https://orcid.org/0000-0003-2527-1598
Felipe Murgas https://orcid.org/0000-0001-9087-1245
Norio Narita https://orcid.org/0000-0001-8511-2981
Greg Olmschenk https://orcid.org/0000-0001-8472-2219
Enric Pallé https://orcid.org/0000-0003-0987-1593
Carina M. Persson https://orcid.org/0000-0003-1257-5146
Adam Popowicz https://orcid.org/0000-0003-3184-5228
Manfred Rätz https://orcid.org/0000-0002-2190-3319
Seth Redfield https://orcid.org/0000-0003-3786-3486
Arno Riffeser https://orcid.org/0000-0002-5466-3892
Marek Skarka https://orcid.org/0000-0002-7602-0046
Luisa Maria Serrano https://orcid.org/0000-0001-9211-3691
Alexis M. S. Smith https://orcid.org/0000-0002-2386-4341
Vincent Van Eylen https://orcid.org/0000-0001-5542-8870
Julian Van Eyken https://orcid.org/0000-0003-2192-5371
Anäel Wünsche https://orcid.org/0000-0002-6176-9847

References

Akeson, R., & Christiansen, J. 2019, AAS, 233, 140.09
Alderson, L., Wakeford, H. R., Alam, M. K., et al. 2023, Natur, 614, 664
Anderson, D. R., Collier Cameron, A., Delrez, L., et al. 2017, A&A, 604, A110
Barlow, T. 2024, MAKEE: MAuna Kea Echelle Extraction, Astrophysics Source Code Library, ascl:2407.001
Barragán, O., Aigrain, S., Rajpaul, V. M., & Zicher, N. 2022, MNRAS, 509, 866
Barragán, O., Gandolfi, D., & Antoniciello, G. 2019, MNRAS, 482, 1017
Batygin, K., Bodenheimer, P. H., & Laughlin, G. P. 2016, ApJ, 829, 114
Beaugé, C., & Nesvorný, D. 2012, ApJ, 751, 119
Becker, J. C., Vanderburg, A., Adams, F. C., Rappaport, S. A., & Schwengeler, H. M. 2015, ApJL, 812, L18
Beleznay, M., & Kunimoto, M. 2022, MNRAS, 516, 75
Birkby, J. L., de Kok, R. J., Brogi, M., Schwarz, H., & Snellen, I. A. G. 2017, AJ, 153, 138
Bouchez, A. H., Dekany, R. G., Angione, J. R., et al. 2008, SPIE, 7015, 70150Z
Breiman, L. 1996, Mach. Learn., 24, 49
Breiman, L. 2001, Mach. Learn., 45, 5
Caldwell, D. A., Jenkins, J. M., & Ting, E. B. 2020, TESS Light Curves From Full Frame Images ("TESS-SPOC"), MAST, doi:10.17909/t9-wpz1-8s54
Charalambous, C., Teyssandier, J., & Libert, A. S. 2022, MNRAS, 514, 3844
Chatterjee, S., Ford, E. B., Matsumura, S., & Rasio, F. A. 2008, ApJ, 686, 580
Choi, J., Dotter, A., Conroy, C., et al. 2016, ApJ, 823, 102
Chontos, A., Murphy, J. M. A., MacDougall, M. G., et al. 2022, AJ, 163, 297
Collins, K. A., Kielkopf, J. F., Stassun, K. G., & Hessman, F. V. 2017, AJ, 153, 77
Cumming, A., Butler, R. P., Marcy, G. W., et al. 2008, PASP, 120, 531
Cyburt, R. H., Fields, B. D., & Olive, K. A. 2003, PhLB, 567, 227
Dawson, R. I., & Johnson, J. A. 2018, ARA&A, 56, 175
Dawson, R. I., Huang, C. X., Lissauer, J. J., et al. 2019, AJ, 158, 65
Deming, D., Louie, D., & Sheets, H. 2019, PASP, 131, 013001
Dodson-Robinson, S. E., Willacy, K., Bodenheimer, P., Turner, N. J., & Beichman, C. A. 2009, Icar, 200, 672
Dong, R., Zhu, Z., & Whitney, B. 2015, ApJ, 809, 93
Dotter, A. 2016, ApJS, 222, 8
Endl, M., & Cochran, W. D. 2016, PASP, 128, 094502
Endl, M., Cochran, W. D., Kürster, M., et al. 2006, ApJ, 649, 436
Endl, M., Kürster, M., Els, S., et al. 2000, A&A, 362, 585
Endl, M., Robertson, P., Cochran, W. D., et al. 2022, AJ, 164, 238
Feroz, F., & Hobson, M. P. 2008, MNRAS, 384, 449
Feroz, F., Hobson, M. P., & Bridges, M. 2009, MNRAS, 398, 1601
Feroz, F., Hobson, M. P., Cameron, E., & Pettitt, A. N. 2019, OJAp, 2, 10
Foreman-Mackey, D., Hogg, D. W., Lang, D., & Goodman, J. 2013, PASP, 125, 306
Fossati, L., Erkaev, N. V., Lammer, H., et al. 2017, A&A, 598, A90
Fressin, F., Torres, G., Charbonneau, D., et al. 2013, ApJ, 766, 81
Friedman, J. H. 2001, Ann. Stat., 29, 1189, https://www.jstor.org/stable/2699986
Fu, G., Espinoza, N., Sing, D. K., et al. 2022, ApJL, 940, L35
Gan, T., Guo, K., Liu, B., et al. 2024, ApJ, 967, 74
Gan, T., Wang, S. X., Wang, W., et al. 2023, AJ, 165, 17
Ge, J., Chen, W., Chen, Y., et al. 2024, ChJSS, 44, 400
Glusman, R. I., Cañas, C. I., Kanodia, S., et al. 2026, AJ, 171, 146
Goldreich, P., & Sari, R. 2003, ApJ, 585, 1024
Griffith, C. A. 2014, RSPTA, 372, 20130086
Gupta, A. F., Fitzmaurice, E., Mahadevan, S., et al. 2025, AJ, 170, 264
Hallatt, T., & Lee, E. J. 2020, ApJ, 904, 134
Halverson, S., Terrien, R., Mahadevan, S., et al. 2016, SPIE, 9908, 99086P
Hasegawa, Y., & Pudritz, R. E. 2013, ApJ, 778, 78
Howard, A. W., Marcy, G. W., Bryson, S. T., et al. 2012, ApJS, 201, 15
Howell, S. B., Matson, R. A., Ciardi, D. R., et al. 2021, yCat, 5161, 0
James, F., & Roos, M. 1975, CoPhC, 10, 343
Jenkins, J. M. 2002, ApJ, 575, 493
Jenkins, J. M., Tenenbaum, P., Seader, S., et al. 2020, Kepler Science Document KSCI-19081-003, Kepler
Jenkins, J. M., Twicken, J. D., McCauliff, S., et al. 2016, SPIE, 9913, 99133E
Kamulali, J., Nsamba, B., Adibekyan, V., et al. 2025, A&A, 695, A57
Kellermann, H., Wang, L., Fahrenschon, V., et al. 2020, SPIE, 11447, 114474K
Kempton, E. M. R., Bean, J. L., Louie, D. R., et al. 2018, PASP, 130, 114401
Kepler, J. 1609, Astronomia Nova (Pragae)
Knutson, H. A., Fulton, B. J., Montet, B. T., et al. 2014, ApJ, 785, 126
Köhler, J., Zechmeister, M., Hatzes, A., et al. 2025, A&A, 698, A44
Kozai, Y. 1962, AJ, 67, 591
Lawson, C. L., & Hanson, R. J. 1995, Solving Least Squares Problems (SIAM)
Li, D., Mustill, A. J., & Davies, M. B. 2019a, MNRAS, 488, 1366
Li, D., Mustill, A. J., & Davies, M. B. 2020, MNRAS, 496, 1149
Li, J., Tenenbaum, P., Twicken, J. D., et al. 2019b, PASP, 131, 024506
Libert, A. S., & Tsiganis, K. 2009, A&A, 493, 677

Lidov, M. L. 1962, P&SS, 9, 719
Lin, D. N. C., Bodenheimer, P., & Richardson, D. C. 1996, Natur, 380, 606
Luger, R., Agol, E., Foreman-Mackey, D., et al. 2019, AJ, 157, 64
Luque, R., Osborn, H. P., Leleu, A., et al. 2023, Natur, 623, 932
Marcy, G., Butler, R. P., Fischer, D., et al. 2005, PThPS, 158, 24
Mayor, M., & Queloz, D. 1995, Natur, 378, 355
Mayor, M., Marmier, M., Lovis, C., et al. 2011, arXiv:1109.2497
Mink, D. J. 2011, ASPC, 442, 305
Mollière, P., Molyarova, T., Bitsch, B., et al. 2022, ApJ, 934, 74
Mordasini, C., Alibert, Y., Benz, W., Klahr, H., & Henning, T. 2012, A&A, 541, A97
Morrell, S., Naylor, T., Southworth, J., & Sing, D. K. 2026, MNRAS, 545, staf2063
Morton, T. D. 2015, isochrones: Stellar model grid package, Astrophysics Source Code Library, ascl:1503.010
Müller, S., & Helled, R. 2023, FrASS, 10, 1179000
Mustill, A. J., Davies, M. B., & Johansen, A. 2015, ApJ, 808, 14
Naoz, S., Farr, W. M., Lithwick, Y., Rasio, F. A., & Teyssandier, J. 2011, Natur, 473, 187
Narita, N., Fukui, A., Kusakabe, N., et al. 2019, JATIS, 5, 015001
Nascimbeni, V., Piotto, G., Börner, A., et al. 2022, A&A, 658, A31
Nelson, R. P., & Papaloizou, J. C. B. 2004, MNRAS, 350, 849
Nesvorný, D., Chrenko, O., & Flock, M. 2022, ApJ, 925, 38
NExScI 2022, Exoplanet Follow-up Observing Program Web Service, doi:10.26134/EXOFOP5
Nsamba, B., Weiss, A., & Kamulali, J. 2025, MNRAS, 536, 2558
Öberg, K. I., Murray-Clay, R., & Bergin, E. A. 2011, ApJL, 743, L16
Parviainen, H., & Aigrain, S. 2015, MNRAS, 453, 3822
Parviainen, H., Palle, E., Zapatero-Osorio, M. R., et al. 2020, A&A, 633, A28
Pascale, E., Bezawada, N., Barstow, J., et al. 2018, SPIE, 10698, 106980H
Passegger, V. M., Suárez Mascareño, A., Allart, R., et al. 2024, A&A, 684, A22
Paxton, B., Bildsten, L., Dotter, A., et al. 2011, ApJS, 192, 3
Paxton, B., Cantiello, M., Arras, P., et al. 2013, ApJS, 208, 4
Paxton, B., Marchant, P., Schwab, J., et al. 2015, ApJS, 220, 15
Paxton, B., Schwab, J., Bauer, E. B., et al. 2018, ApJS, 234, 34
Paxton, B., Smolec, R., Schwab, J., et al. 2019, ApJS, 243, 10
Pepper, J., Rodriguez, J. E., Collins, K. A., et al. 2017, AJ, 153, 215
Petigura, E. A., Marcy, G. W., Winn, J. N., et al. 2018, AJ, 155, 89
Petrovich, C. 2015a, ApJ, 799, 27
Petrovich, C. 2015b, ApJ, 805, 75
Pinamonti, M., Sozzetti, A., Maldonado, J., et al. 2022, A&A, 664, A65
Prokhorenkova, L., Gusev, G., Vorobev, A., Dorogush, A. V., & Gulin, A. 2017, arXiv:1706.09516
Puig, L., Pilbratt, G., Heske, A., et al. 2018, ExA, 46, 211
Rasio, F. A., & Ford, E. B. 1996, Sci, 274, 954
Rauer, H., Aerts, C., Deleuil, M., et al. 2022, EPSC, 16, 453
Rey, J., Bouchy, F., Stalport, M., et al. 2018, A&A, 619, A115
Ricker, G. R., Winn, J. N., Vanderspek, R., et al. 2014, SPIE, 9143, 914320
Rustamkulov, Z., Sing, D. K., Mukherjee, S., et al. 2023, Natur, 614, 659
Sabotta, S., Kabath, P., Korth, J., et al. 2019, MNRAS, 489, 2069
Sabotta, S., Schlecker, M., Chaturvedi, P., et al. 2021, A&A, 653, A114
Schlafly, E. F., & Finkbeiner, D. P. 2011, ApJ, 737, 103
Schlegel, D. J., Finkbeiner, D. P., & Davis, M. 1998, ApJ, 500, 525
Schwab, C., Rakich, A., Gong, Q., et al. 2016, SPIE, 9908, 99087H
Sebastian, D., Guenther, E. W., Deleuil, M., et al. 2022, MNRAS, 516, 636
Shulyak, D., Rengel, M., Reiners, A., Seemann, U., & Yan, F. 2019, A&A, 629, A109
Tanaka, H., Takeuchi, T., & Ward, W. R. 2002, ApJ, 565, 1257
Tayar, J., Claytor, Z. R., Huber, D., & van Saders, J. 2022, ApJ, 927, 31
Thomas, L., Hébrard, G., Kellermann, H., et al. 2025, A&A, 694, A143
Tinetti, G., Drossart, P., Eccleston, P., et al. 2016, SPIE, 9904, 99041X
Tran, Q. H., Bowler, B. P., Cochran, W. D., et al. 2025, AJ, 170, 103
Tull, R. G., MacQueen, P. J., Sneden, C., & Lambert, D. L. 1995, PASP, 107, 251
Twicken, J. D., Catanzarite, J. H., Clarke, B. D., et al. 2018, PASP, 130, 064502
Vines, J. I., & Jenkins, J. S. 2022, MNRAS, 513, 2719
Wang, J., Fischer, D. A., Horch, E. P., & Huang, X. 2015, ApJ, 799, 229
Wang, X.-Y., Wang, Y.-H., Wang, S., et al. 2021, ApJS, 255, 15
Ward, W. R. 1997, Icar, 126, 261
Wehenkel, L., Ernst, D., & Geurts, P. 2006, in Proc. Robust Methods for Power System State Estimation and Load Forecasting (Liege Universite) https://hdl.handle.net/2268/13447
Winn, J. N., & Fabrycky, D. C. 2015, ARA&A, 53, 409
Wolpert, D. 1992, NN, 5, 241
Wright, J. T., Fakhouri, O., Marcy, G. W., et al. 2011, PASP, 123, 412
Wu, Y., & Lithwick, Y. 2011, ApJ, 735, 109
Wu, Y., & Murray, N. 2003, ApJ, 589, 605
Yee, S. W., Stefánsson, G., Thorngren, D., et al. 2025, AJ, 169, 225
Yu, H., & Dai, F. 2024, ApJ, 972, 159
Yu, L., Zhou, G., Rodriguez, J. E., et al. 2018, AJ, 156, 250
Zechmeister, M., Köhler, J., & Chamarthi, S. 2021, viper: Velocity and IP EstimatoR, Astrophysics Source Code Library, ascl:2108.006